









Chicxulub impact structure, IODP-ICDP Expedition 364 drill core: Geochemistry of the granite basement

Jean-Guillaume FEIGNON ^{1*}, Sietze J. DE GRAAFF ^{2,3}, Ludovic FERRIÈRE ⁴, Pim KASKES ^{2,3}, Thomas DÉHAIS ^{2,3}, Steven GODERIS ², Philippe CLAEYS ², and Christian KOEBERL ¹

¹Department of Lithospheric Research, University of Vienna, Althanstrasse 14, Vienna A-1090, Austria

²Research Unit: Analytical, Environmental & Geo-Chemistry, Department of Chemistry, Vrije Universiteit Brussel, AMGC-WE-VUB, Pleinlaan 2, Brussels 1050, Belgium

³Laboratoire G-Time, Université Libre de Bruxelles, Av. F.D. Roosevelt 50, Brussels 1050, Belgium

⁴Natural History Museum, Burgring 7, Vienna A-1010, Austria

*Corresponding author. E-mail: jean-guillaume.feignon@univie.ac.at

(Received 24 November 2020; revision accepted 28 May 2021)

Abstract—The IODP-ICDP Expedition 364 drilling recovered a 829 m core from Hole M0077A, sampling ~600 m of near continuous crystalline basement within the peak ring of the Chicxulub impact structure. The bulk of the basement consists of pervasively deformed, fractured, and shocked granite. Detailed geochemical investigations of 41 granitoid samples, that is, major and trace element contents, and Sr–Nd isotopic ratios are presented here, providing a broad overview of the composition of the granitic crystalline basement. Mainly granite but also granite clasts (in impact melt rock), granite breccias, and aplite were analyzed, yielding relatively homogeneous compositions between all samples. The granite is part of the high-K, calc-alkaline metaluminous series. Additionally, they are characterized by high Sr/Y and (La/Yb)_N ratios, and low Y and Yb contents, which are typical for adakitic rocks. However, other criteria (such as Al₂O₃ and MgO contents, Mg#, K₂O/Na₂O ratio, Ni concentrations, etc.) do not match the adakite definition. Rubidium–Sr errorchron and initial ⁸⁷Sr/⁸⁶Sr_{t=326Ma} suggest that a hydrothermal fluid metasomatic event occurred shortly after the granite formation, in addition to the postimpact alteration, which mainly affected samples crosscut by shear fractures or in contact with aplite, where the fluid circulation was enhanced, and would have preferentially affected fluid-mobile element concentrations. The initial (ε_{Nd})_{t=326Ma} values range from –4.0 to 3.2 and indicate that a minor Grenville basement component may have been involved in the granite genesis. Our results are consistent with previous studies, further supporting that the cored granite unit intruded the Maya block during the Carboniferous, in an arc setting with crustal melting related to the closure of the Rheic Ocean associated with the assembly of Pangea. The granite was likely affected by two distinct hydrothermal alteration events, both influencing the granite chemistry: (1) a hydrothermal metasomatic event, possibly related to the first stages of Pangea breakup, which occurred approximately 50 Myr after the granite crystallization, and (2) the postimpact hydrothermal alteration linked to a long-lived hydrothermal system within the Chicxulub structure. Importantly, the granites sampled in Hole M0077A are unique in composition when compared to granite or gneiss clasts from other drill cores recovered from the Chicxulub impact structure. This marks them as valuable lithologies that provide new insights into the Yucatán basement.

INTRODUCTION

The ~200 km diameter (e.g., Gulick et al. 2013) and 66.05 Myr old (Sprain et al. 2018) Chicxulub impact structure is located in the northwestern part of the Yucatán peninsula (Mexico, Fig. 1). The characterization of shocked quartz grains in samples derived from within the structure confirmed its impact origin (Penfield and Camargo 1981; Hildebrand et al. 1991). Chicxulub is the only known terrestrial impact structure with a nearly intact, well-preserved peak ring (e.g., Morgan et al. 1997, 2016) and it is related to the Cretaceous–Paleogene boundary and the non-avian dinosaur extinction (Swisher et al. 1992; Smit 1999; Schulte et al. 2010; Chiarenza et al. 2020; Goderis et al. 2021). The structure was formed by the impact of an ~12 km diameter carbonaceous chondrite-like body (Shukolyukov and Lugmair 1998; Quitté et al. 2007; Goderis et al. 2013; Collins et al. 2020) on an ~3 km thick Mesozoic carbonate and evaporite platform overlying crystalline basement rock (e.g., Morgan et al. [2016] and references therein).

Today, the impact structure is buried under ~1 km of Cenozoic limestones, with its only surface expression being a ring of cenotes (i.e., water-filled sinkholes). Consequently, the direct study of the different lithologies occurring in the impact structure (i.e., a variety of impact breccias, impact melt rocks, and (shocked) pre-impact basement rocks) is only possible either by investigating ejecta material (Belza et al. 2015) or by using samples recovered by scientific drilling programs (e.g., Koeberl and Sigurdsson 1992; Koeberl 1993a; Belza et al. 2012) or petroleum exploration campaigns (e.g., Lopez Ramos 1975; Hildebrand et al. 1991; Swisher et al. 1992; Urrutia-Fucugauchi et al. 1996; Claeys et al. 2003; Tuchscherer et al. [2004a] and references therein). Drilling campaigns were conducted within the impact structure by *Petróleos Mexicanos* (PEMEX), recovering the Chicxulub–1 (C–1) and Yucatan–6 (Y6) cores, which sampled melt-bearing impact breccia (suevite) and impact melt rock (e.g., Hildebrand et al. 1991; Kring and Boynton 1992; Swisher et al. 1992; Schuraytz et al. 1994; Ward et al. 1995; Claeys et al. 2003; Kettrup and Deutsch 2003); and by the International Continental Scientific Drilling Program (ICDP), recovering the Yaxcopoil–1 (Yax–1) core (e.g., Tuchscherer et al. 2004a, 2004b, 2005, 2006).

Pre-impact basement material was generally found as clasts in the suevite units recovered in previous drill core campaigns, with a wide variety of target lithologies being reported, including Cretaceous sedimentary platform rocks (a 616 m thick megablock of limestones, dolomites, and anhydrites was identified in the Yax–1 drill core, e.g., Dressler et al. 2003; Wittmann et al. 2004; Belza et al. 2012), granites, orthogneisses, amphibolites, quartzites,

quartz-mica schists, and dolerites (e.g., Sharpton et al. 1992; Kettrup et al. 2000; Claeys et al. 2003; Kettrup and Deutsch 2003; Schmitt et al. 2004; Tuchscherer et al. 2005). Importantly, no large unit of the underlying crystalline basement material was ever recovered in any of the previous drill core campaigns.

A large crystalline basement unit composed mainly of granite was recovered for the first time in the Chicxulub peak ring drilled during the joint International Ocean Discovery Program (IODP) and ICDP Expedition 364 (see the IODP-ICDP Expedition 364 Drill Core section and Morgan et al. 2017). This unit represents the main focus of this study. In order to better characterize the granite basement, we present the results of the major and trace element analyses of 41 granitoid samples, including Sr–Nd isotopic analyses for 16 samples, from the “lower peak ring” section. A comparison with chemical data for granites and granitic gneisses from previous studies is also presented. Our investigations of a large set of granite samples offer a unique opportunity to constrain the chemistry and sources of the granite, a major component to the impactites recovered in the drill core; how it was affected by the impact event; and, more generally, refine the Yucatán basement geology.

THE CHICXULUB IMPACT STRUCTURE

Geological Setting

The crystalline basement rocks forming the Yucatán platform belong to the Maya block (Fig. 1), which is generally described as encompassing the Yucatán peninsula, the northeast of Mexico, the coastal plains of the western and northern Gulf of Mexico, and the Chiapas massif complex (Keppie et al. 2011; Weber et al. 2012, 2018), with its north and northeastern boundaries bordered by continental shelves and oceanic lithosphere (Alaniz-Álvarez et al. 1996; Keppie et al. 2011). The Maya block was thought to be bordered in the northwest by the Oaxaquia block (Grenvillian-aged); in the southwest by the Cuicateco complex; and in the south by the Polochic, Motagua, and Jocotlán-Chamaleón fault systems (Fig. 1), making the separation with the Caribbean plate (Dengo 1969; Donnelly et al. 1990; Weber et al. 2012, 2018). However, the exact geographical area covered by the Maya block remains a topic of discussion. Indeed, the work by Ortega-Gutiérrez et al. (2018) suggests that the Chiapas massif (or Southern Maya) forms a distinct lithotectonic domain (Fig. 1), characterized by the presence of medium- to high-grade metamorphic rock outcrops that were not observed in the Maya block (Weber et al. 2008; Ortega-Gutiérrez et al. 2018). The

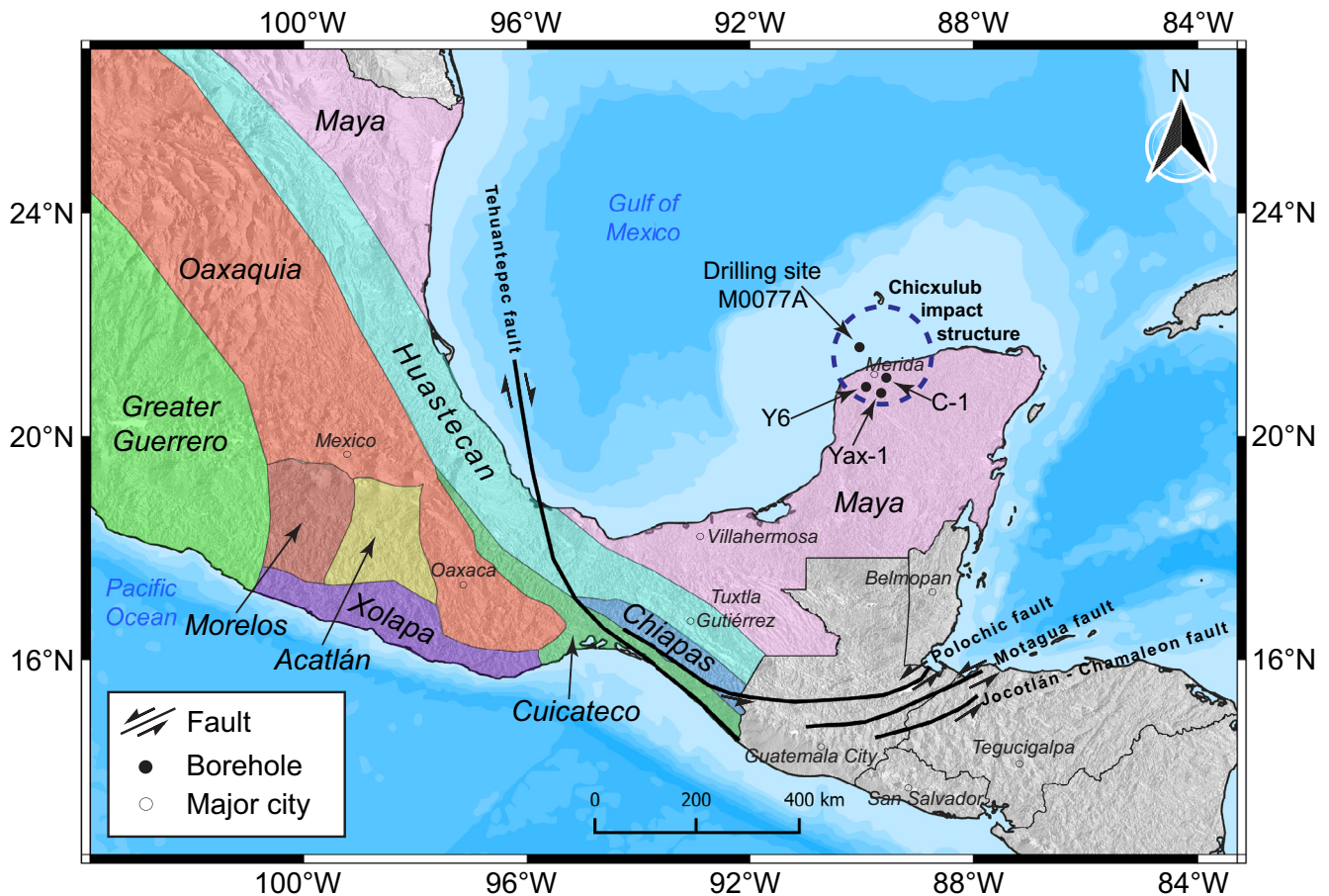


Fig. 1. Map of southeast Mexico with the main tectonostratigraphic domains proposed by Ortega-Gutiérrez et al. (2018), major faults, and the Chicxulub impact structure (dashed circle; 200 km in diameter) with the IODP-ICDP Expedition 364 (M0077A) and previous drilling (Y6, Yax-1, and C-1) locations reported (modified from Weber et al. 2012, 2018; Ortega-Gutiérrez et al. 2018). SRTM data can be found online at: <https://www2.jpl.nasa.gov/srtm/cbanddataproducts.html>. (Color figure can be viewed at wileyonlinelibrary.com.)

Chiapas massif would be separated from the Maya block by the Paleozoic-aged Huastecan orogenic belt. This orogenic system is mostly buried and extends from the Ouachita suture belt in Northwest Mexico to the Polochic, Motagua, and Jocotlán-Chamaleón fault systems in Guatemala. Consequently, the Huastecan orogenic belt separates the Maya block from the Oaxaquia and Cuicateco terranes in the west and southwest, respectively (Fig. 1).

The material composing the Maya block is mainly Pan-African-aged, such as tholeiitic dolerite intruded in Grenvillian Novillo gneiss in the Cd. Victoria area, yielding an Ar/Ar age of 546 ± 5 Ma (Keppie et al. 2011). In addition, the age of zircon grains found in ejected material at various K–Pg boundary locations and from boreholes inside the Chicxulub impact structure range mainly between 550 and 545 Ma, just after the Cambrian–Precambrian boundary (Krogh

et al. 1993; Kettrup and Deutsch [2003] and references therein; Kamo et al. 2011; Keppie et al. 2011), suggesting that a predominantly late Ediacaran crystalline basement constitutes the northern part of the Yucatán peninsula (Ortega-Gutiérrez et al. 2018). The Sm–Nd T_{DM} model ages reported from orthogneisses, impact melt rock, impact glass, and amphibolites display a wide range between 1.4 and 0.7 Ga, suggesting the involvement of a Grenvillian component during the formation of Yucatán crystalline basement (Kettrup and Deutsch 2003; Keppie et al. 2011). Granites and zircon grains with younger ages (late Paleozoic, ~320–345 Ma) are also reported, but are comparatively rare (Kamo and Krogh 1995; Kamo et al. 2011; Keppie et al. 2011).

While the exact extent of the lithotectonic domains remains up for debate, paleomagnetic reconstructions indicate that the Maya block, and more precisely the Yucatán–Chiapas block, separated from Texas (southern

margin of Laurentia) during the breakup of Pangea during the Late Triassic (~230 Ma). The Yucatán-Chiapas block then rotated ~40° (up to 60° for the Yucatán basement, independently from the Chiapas block) anticlockwise as the Gulf of Mexico opened. The rotation was accommodated by the presence of a transform fault marking the boundary between continental and oceanic crust offshore the east coast of Mexico (Dickinson and Lawton 2001; Steiner 2005). The seafloor spreading began during the Callovian (~164 Ma). The rotation ceased by the Berriasian (~139 Ma), and, since then, the Yucatán block has remained geologically stable (see detailed geotectonic reconstructions in Dickinson and Lawton 2001; Steiner [2005] and references therein). At the time of the Chicxulub impact event, at ~66.05 Ma (Sprain et al. 2018), the Yucatán basement was covered by an approximately 3 km thick carbonate platform composed of limestone, dolomite, marl, and anhydrite (Lopez Ramos 1975; Kring 2005). Additionally, the platform was covered by seawater, deepening to the north and northeast with an average water depth of ~600 m (Gulick et al. 2008).

During the impact event, the target rocks (sedimentary rocks and the underlying basement rocks) were either vaporized, melted, shocked, ejected from the crater, uplifted, injected as melt into the structure, and/or incorporated into gravity flows during crater modification (Morgan et al. 2016; Gulick et al. 2019; de Graaff et al. 2021). Rock fluidization rapidly led to the formation of a central peak ring inside the structure (Riller et al. 2018; Rae et al. 2019). Afterward, the peak ring was intensively altered by a long-lived, by more than one million years, hydrothermal system (Kring et al. 2020).

The impact structure site was finally covered by carbonates and evaporites from the Cretaceous to the Quaternary, forming the current subsurface geology of the Yucatán peninsula (Lopez Ramos 1975; Hildebrand et al. 1991), and preserving the impact structure and its peak ring from erosion.

IODP-ICDP Expedition 364 Drill Core

Investigating the rocks that make up the peak ring in order to understand its nature, chemistry, and origin, as well as its formation mechanism, was one of the primary goals of the IODP-ICDP Expedition 364 (e.g., Morgan et al. 2017). A continuous core from Hole M0077A (see Fig. 2) was recovered between 505.7 and 1334.7 mbsf (meters below sea floor). Four main lithological units were identified, including (1) a “postimpact” Cenozoic sedimentary rock section (from 505.7 to 617.3 mbsf); (2) a melt-bearing, polymict, impact breccia (suevite) section (from 617.3 to

721.6 mbsf); overlaying (3) an impact melt rock and green schlieren unit (from 721.6 to 747.0 mbsf), or “upper impact melt rock” unit (Morgan et al. 2017; de Graaff et al. 2021). The lower and thicker recovered unit (4), the so-called “lower peak ring” section (from 747.0 to 1334.7 mbsf), consists of granitoid (coarse-grained granite with centimeter to decimeter aplite and pegmatite facies areas) intruded by several pre-impact subvolcanic dikes and intercalations of millimeter to decimeter suevite-like breccia and impact melt rocks (Morgan et al. 2017). The latter has been discussed in detail, and referred to as the “lower impact melt-bearing unit” (LIMB), by de Graaff et al. (2021).

The “lower peak ring” section represents a large, nearly uninterrupted crystalline basement rock unit, and is the main focus of this study. The occurrence of crystalline basement rocks at such relatively shallow depths suggests that they were uplifted from a pre-impact depth of 8–10 km (Morgan et al. 2016; Riller et al. 2018). The basement rocks are shocked, with most of the minerals showing signs of shock metamorphism. Shock pressures experienced by the granite were estimated between ~16 and 18 GPa (Feignon et al. 2020).

Zhao et al. (2020) reported on the investigation of nine granite samples and suggested that these late Paleozoic granites are K-rich adakitic rocks that formed following the melting of a thickened crust with a residue of garnet-bearing amphibolite or garnet-bearing granulite. However, the term “adakitic” should be used with care in this context, as a full set of criteria should be used in addition to the used Sr/Y and La/Yb ratios to define an adakitic rock (see Moyen 2009). The long-lasting hydrothermal system, which occurred within Chicxulub (e.g., Kring et al. 2020), may also have had a significant effect on the bulk granite geochemistry as also suggested by de Graaff et al. (2021).

Granite Ages

Dating on the Hole M0077A granites was performed on zircon and yield late Paleozoic (Carboniferous) U–Pb ages of 326 ± 5 Ma (Rasmussen et al. 2019; Zhao et al. 2020) and 334 ± 2.3 Ma (Ross et al. 2021). More recent ages (215 ± 28 to 260 ± 9 Ma) were obtained for allanite and probably recorded allanite growth during alteration events, while zircon ages represent the igneous crystallization (Wittmann et al. 2018). A similar late Paleozoic age, albeit with large uncertainty, of 478 ± 110 Ma, was obtained in zircons from Yax–1 impact breccia (Schmieder et al. 2017). These ages contrast the mostly dominant Pan-African-aged zircon population recovered from K–Pg boundary sites and previous drill cores (e.g., Krogh et al. 1993; Kamo et al. 2011; Keppie et al. 2011).

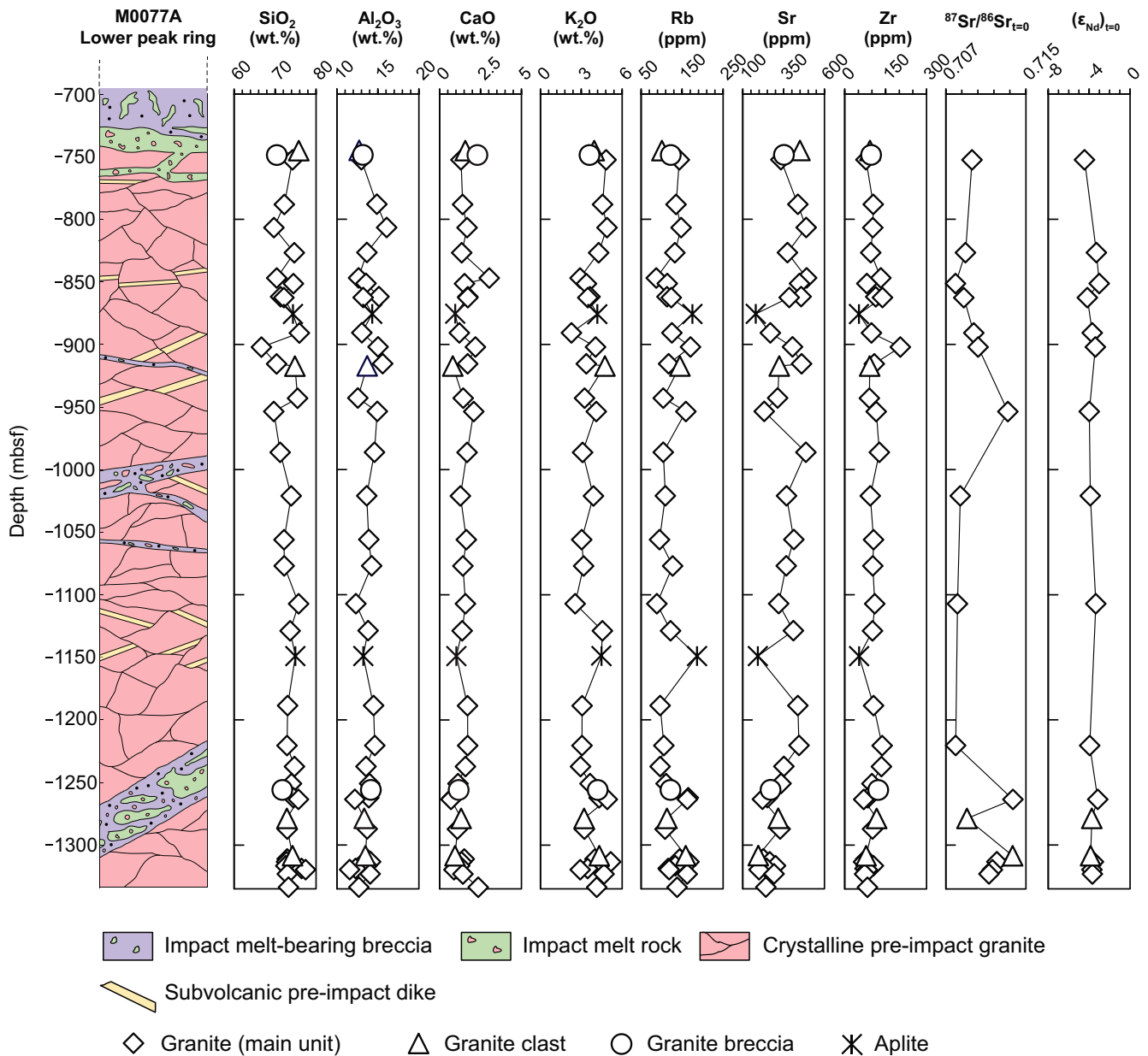


Fig. 2. Lithostratigraphy of the “lower peak ring” section (747.0–1334.7 mbsf) of the Hole M0077A core (from de Graaff et al. 2021), comparing the concentration variations of selected major (SiO₂, Al₂O₃, CaO, K₂O), trace elements (Rb, Sr, Zr), and Sr–Nd isotopic compositions with depth in the investigated samples. (Color figure can be viewed at wileyonlinelibrary.com.)

Using the ages presented in both Zhao et al. (2020) and Ross et al. (2021), we can assume that these granites were probably emplaced during the Carboniferous. During this period, the Yucatán block was located at the edge of the Gondwana craton and recorded arc magmatism originating from the subduction of oceanic crust of the Rheic ocean beneath the northern edge of Gondwana before its collision with Laurentia (Pangean assembly) according to the geotectonic reconstructions of Dickinson and Lawton (2001).

MATERIALS AND METHODS

Sample Selection

Forty-one samples ranging from 20 to 50 g in mass were prepared from a selected number of granitoid samples taken at regular intervals between 745.1 and 1334.7 mbsf. Sample nomenclature used in this study corresponds to Core#Section#_Top(cm)–Bottom(cm) and indicates the exact sampling interval as defined in Morgan et al. (2017), while the centimeters indicate the

distance in a core section from the top. The uppermost sample consists of a granite clast located in the upper impact melt rock (Unit 3), whereas the other samples were taken from the “lower peak ring” section. Due to the size of core samples (8 cm diameter), special care was taken to select representative equigranular granite samples to assess any compositional variation with core depth; texture change; and the effects of shock, fracturing, and other types of chemical alteration as well as the fluid circulation following the onset of the hydrothermal system. As such, three samples exhibiting a porphyritic texture (with large K-feldspar crystals up to 7 cm in size) were excluded from the scope of this study, as their chemistry would be biased by K-feldspar accumulation rather than representing whole rock composition.

The majority of the selected samples ($n = 33$) were taken from the main granite unit (i.e., granites sampled from the continuous granite interval of at least 1 m in thickness). In addition, samples of granite clasts in impact melt rock ($n = 4$), one from the “upper impact melt rock” and the remaining three from the LIMB, were selected. A granite clast was considered in this study as having a size smaller than one meter throughout the drill core. Additionally, two granite breccias as well as two aplites were selected to assess any chemical variation related to petrographic textures. Sample locations and their relative depths within the core are shown in Fig. 2 and Table 1.

Petrographic Investigations

Polished thin sections of the samples were prepared and investigated for their mineralogy, textures, and shock metamorphic features in minerals using optical microscopy at the University of Vienna and a JEOL JSM-6610 variable pressure (VP) scanning electron microscope (SEM) at the Natural History Museum (Vienna, Austria). Additionally, detailed investigations on shocked quartz grains were made on 11 thin sections using a universal stage (see Feignon et al. 2020).

Major Element Mapping

Energy-dispersive micro X-ray fluorescence (μ XRF) was performed on 20 granite samples at the Vrije Universiteit Brussels (VUB) using a Bruker M4 Tornado benchtop μ XRF surface scanner equipped with an Rh tube as X-ray source and two XFlash 430 Silicon Drift detectors. This technique produced high-resolution elemental distribution maps by scanning flat sample surfaces (i.e., polished thin and thick sections), in a rapid, nondestructive, and cost-efficient way (e.g., de Winter and Claeys 2016; Kaskes et al. 2021). The μ XRF

mapping was performed with two detectors and maximized X-ray source energy settings (50 kV and 600 μ A, without any filter). The measurements were carried out under near vacuum conditions (20 mbar) with a spatial resolution of 25 μ m and an integration time of 1 ms per 25 μ m. This approach resulted in qualitative multi-element maps and semiquantitative single-element heat maps, in which the highest spectral peak for one element (i.e., the largest number of counts below the—in general— $K\alpha$ peak) corresponds to the pixel in the sample with the highest possible RGB value (i.e., 255).

Geochemical Analysis

The samples were crushed in polyethylene wrappers and then powdered in an agate bowl using a Retsch RS200 vibratory disk mill. The obtained sample powders were then stored in clean, hermetically sealed, polyethylene vials.

Major Element Analysis

Samples were measured by means of glass bead-based X-ray fluorescence (XRF). The analyses were performed using an X-ray spectrometer PHILIPS PW2404 at the Department of Lithospheric Research (University of Vienna, Austria) with a super sharp end window tube and an Rh-anode. The element concentrations were determined using calibration curves established using international reference materials. Accuracy and precision values (in wt%) are about 0.6 for SiO_2 and Fe_2O_3 , 0.3 for Al_2O_3 , 0.2 for Na_2O , 0.07 for MgO and CaO , 0.03 for TiO_2 and K_2O , 0.02 for P_2O_5 , and 0.01 for MnO .

Approximately 3 g of homogenized rock powder was weighed in a porcelain crucible that was previously heated at 1050 °C for at least 3 h and cooled down to room temperature in a desiccator. For LOI determination, the crucible with rock powder was placed into an oven at 110 °C overnight, and weighed again. Next, the crucible with rock powder was placed into a muffle furnace at 850 °C for 3 h, and weighed one final time. The LOI was then calculated.

Fused beads were prepared by adding 0.8 g of the calcined sample powder to 8.0 g of a di-lithium tetraborate and di-lithium metaborate (Fluxana FX-X65-2) mixture (2:1 ratio). This mixture was then poured into a crucible of platinum and gold and fused using a PANalytical EAGON 2 furnace.

Trace Element Analysis

Trace element concentrations were both measured using bulk XRF and instrumental neutron activation analysis (INAA). The bulk XRF measurement for trace element concentrations was done on pressed powder

Table 1. Major element concentrations (in wt%) of all the investigated samples from the Expedition 364 Chicxulub drill core, namely granites (from the main unit), granite clasts, granite breccias, and aplites, as determined using bulk XRF.

Sample	Depth (mbsf)	SiO ₂	TiO ₂	Al ₂ O ₃	Fe ₂ O ₃ *	MnO	MgO	CaO	Na ₂ O	K ₂ O	P ₂ O ₅	LOI	Total	K ₂ O/Na ₂ O	A/CNK	Mg#
Granites (from the main unit)																
97R3_10-12.5	752.5	74.3	0.16	13.0	1.07	0.02	0.46	1.31	3.71	4.82	0.05	1.06	99.90	1.30	0.94	40
110R2_14-16	788.1	72.3	0.21	14.9	1.09	0.02	0.47	1.41	4.82	4.56	0.05	b.d.l.	99.76	0.95	0.96	40
116R2_58-62	806.7	69.7	0.21	16.1	1.28	0.02	0.61	1.68	4.75	4.88	0.07	1.34	100.63	1.03	0.99	42
125R1_40-42.5	826.7	74.7	0.14	13.7	0.90	0.01	0.36	1.36	4.36	4.27	0.04	0.52	100.31	0.98	0.96	38
134R3_75-79	846.9	70.4	0.26	12.6	1.60	0.04	1.32	3.04	4.52	2.91	0.08	2.28	99.10	0.64	0.78	56
136R2_20-25	851.4	74.5	0.12	13.5	0.67	0.01	0.33	1.53	4.67	3.38	0.03	1.08	99.85	0.72	0.96	43
142R2_105-109	861.9	71.4	0.20	15.1	1.50	0.02	0.62	1.73	5.05	3.64	0.07	0.01	99.32	0.72	0.98	39
142R3_48-50	862.6	72.2	0.38	13.2	2.55	0.04	0.94	1.73	4.23	3.48	0.20	0.70	99.60	0.82	0.95	36
153R1_47-50.5	890.8	75.9	0.24	13.0	1.04	0.01	0.56	1.21	5.38	2.27	0.10	1.04	100.81	0.42	0.96	45
156R3_11-15	902.1	66.7	0.48	15.0	3.76	0.06	1.35	2.19	4.93	4.04	0.34	0.49	99.32	0.82	0.91	36
163R1_76-77.5	915.5	70.4	0.22	15.6	1.47	0.02	0.61	1.72	5.41	3.37	0.09	0.62	99.47	0.62	0.99	39
172R1_118-121	942.9	75.5	0.15	12.6	0.83	0.02	0.36	1.45	4.41	3.24	0.04	1.10	99.64	0.73	0.94	40
176R2_112-116	953.6	69.7	0.26	14.9	1.50	0.02	0.55	2.09	4.04	4.10	0.09	2.64	99.89	1.01	1.00	36
188R2_11-13.5	986.2	71.3	0.27	14.6	1.82	0.03	0.74	1.68	5.22	3.09	0.13	0.67	99.48	0.59	0.97	38
200R3_12.5-15	1021.0	73.9	0.24	13.6	1.23	0.02	0.49	1.27	4.28	3.89	0.05	1.05	100.10	0.91	1.01	38
212R1_129-131.5	1056.0	72.2	0.19	13.9	1.28	0.02	0.57	1.64	4.90	3.03	0.04	1.21	98.95	0.62	0.97	41
219R1_105.5-108	1077.0	72.2	0.21	14.2	1.48	0.04	0.62	1.43	5.24	3.17	0.06	0.64	99.34	0.60	0.97	39
229R2_62-67	1107.2	75.8	0.21	12.3	1.32	0.03	0.59	1.58	4.30	2.55	0.07	1.15	99.87	0.59	0.97	41
236R1_90-92.5	1128.8	73.7	0.20	13.8	1.29	0.02	0.56	1.38	3.89	4.55	0.06	0.60	100.05	1.17	1.00	40
256R1_70-72.5	1188.6	73.1	0.20	14.5	1.57	0.02	0.66	1.71	5.08	3.06	0.07	0.60	100.51	0.60	0.98	39
266R2_95.5-98.5	1220.5	72.9	0.29	14.6	1.74	0.02	0.61	1.72	5.01	3.05	0.11	0.47	100.55	0.61	1.00	35
272R1_28-30.5	1237.2	74.8	0.26	13.5	1.58	0.02	0.56	1.58	5.01	2.94	0.09	0.77	101.10	0.59	0.95	35
276R2_62-64.5	1250.9	74.0	0.18	14.0	1.26	0.01	0.55	1.13	5.03	3.64	0.06	0.69	100.55	0.72	0.98	40
280R1_47-49	1262.2	74.5	0.13	13.9	0.96	0.03	0.36	0.78	4.52	4.30	0.04	0.57	100.04	0.95	1.03	37
280R2_51.5-53.5	1263.5	75.7	0.13	12.2	0.87	0.01	0.33	0.70	3.80	4.91	0.06	0.46	99.15	1.29	0.95	37
288R1_61-64	1287.2	73.0	0.19	13.7	1.14	0.02	0.51	1.09	5.42	3.22	0.07	0.44	98.80	0.59	0.95	41
296R1_116-118	1311.1	73.0	0.16	13.7	1.28	0.03	0.30	1.51	4.50	4.00	0.07	1.29	99.78	0.89	0.94	26
297R1_36-38	1313.4	72.8	0.14	14.1	1.23	0.01	0.29	1.35	4.22	5.16	0.05	1.25	100.62	1.22	0.94	27
298R1_41-43	1316.5	72.6	0.23	13.7	1.25	0.02	0.48	1.23	4.66	4.29	0.09	1.04	99.56	0.92	0.94	37
298R3_1.5-3.5	1318.7	76.5	0.13	12.3	0.71	0.01	0.28	1.05	4.38	3.46	0.04	0.83	99.63	0.79	0.95	38
299R1_52.5-55	1319.7	77.5	0.16	11.6	1.22	0.02	0.56	0.88	4.01	2.92	0.08	1.04	99.89	0.73	1.02	41
300R1_78-79.5	1323.1	73.0	0.17	14.1	0.91	0.02	0.25	1.43	4.46	4.67	0.06	1.33	100.35	1.05	0.94	30
303R2_82-84.5	1333.7	73.3	0.16	12.7	0.59	0.01	0.14	2.37	4.11	4.13	0.08	1.93	99.49	1.00	0.82	27
Granite clasts																
95R2_19-22	745.1	75.8	0.19	12.7	0.94	b.d.l.	0.63	1.57	3.82	3.95	0.09	0.53	100.23	1.03	0.95	51
163R3_52-57	917.3	74.8	0.19	13.7	0.94	0.01	0.61	0.81	4.11	4.73	0.06	0.71	100.70	1.15	1.03	50

Table 1. *Continued.* Major element concentrations (in wt%) of all the investigated samples from the Expedition 364 Chicxulub drill core, namely granites (from the main unit), granite clasts, granite breccias, and aplites, as determined using bulk XRF.

Sample	Depth (mbsf)	SiO ₂	TiO ₂	Al ₂ O ₃	Fe ₂ O ₃ *	MnO	MgO	CaO	Na ₂ O	K ₂ O	P ₂ O ₅	LOI	Total	K ₂ O/Na ₂ O	A/CNK	Mg#
285R2_26–28.5	1278.7	72.9	0.24	13.3	1.69	0.02	0.64	1.32	5.13	3.20	0.11	0.45	99.00	0.62	0.93	37
295R2_51–53	1308.5	74.3	0.13	13.5	1.01	0.01	0.26	0.95	4.36	4.32	0.05	0.80	99.61	0.99	0.99	28
Granite breccias																
96R2_50–52	748.7	70.5	0.23	13.2	1.62	0.04	1.10	2.32	4.39	3.61	0.08	2.14	99.15	0.82	0.86	51
1278R1_43–45	1256.0	71.8	0.22	14.1	1.69	0.02	0.67	1.17	4.90	4.21	0.10	0.53	99.43	0.86	0.96	38
Aplites																
147R2_0–3	875.7	74.4	0.05	14.3	0.55	0.01	0.07	0.96	5.12	4.17	0.02	0.54	100.17	0.81	0.97	16
242R3_23–26	1149.0	75.0	0.09	13.2	0.59	0.02	0.15	1.03	4.37	4.48	0.03	0.66	99.60	1.03	0.95	28

b.d.l. = below detection limit; LOI = loss on ignition.

*Iron oxide reported as total ferrous Fe.

pellets. The latter were prepared by mixing 0.5 mL of an aqueous polyvinyl alcohol solution (MERCK Mowiol) and approximately 10 g of non-ignited rock powder. The mixture was then placed in a hydraulic press, applying a pressure of approximately 16 tons per square centimeter. The pressed powder pellets were then dried in an oven at 70 °C overnight. Tool cleaning was done using acetone. The trace element concentrations were then obtained by using the intensities at peak and background positions, which were measured on blank specimens for interpolating background intensity at the peak position (Nisbet et al. 1979).

For bulk INAA analysis, between 100 and 150 mg of dried rock powder was placed in small polyethylene vials that were sealed to avoid any leaking of material and/or radioactive contamination after irradiation. The same was done for international reference materials (standards ACE granite, ALL Allende carbonaceous chondrite meteorite, and SDO-1 shale) but using less material (60–90 mg). Samples were then packed in groups of 17, to which three standard samples were added.

Samples and standards were irradiated together for 8 h in the 250 kW Triga reactor of the Atomic Institute of the Austrian Universities at a neutron flux of $2 \times 10^{12} \text{ n cm}^{-2} \text{ s}^{-1}$. Samples and standards were then measured with coaxial Canberra HpGe detectors in three cycles (L1, L2, and L3). The cycle L1 was measured ~5 days after irradiation. Each sample is measured for at least 60 min. Cycle L2 was done ~10 days after irradiation, with ~3–4 h measuring time for each sample. Finally, the Cycle L3 was performed 3–4 weeks after irradiation and the samples were measured for at least 12 h (generally 24 h in this study). Data obtained were then processed automatically by computer, and neutron flux correction was applied. Finally, the data were checked manually. Replicate analysis of international reference materials ACE, ALL, and SDO-1 ($n = 8$) yielded reproducibilities for trace element contents on the order of ~2 to 15 rel%. More details on instrumentation, accuracy, and precision of this method can be found in, for example, Koeberl (1993b), Son and Koeberl (2005), and Mader and Koeberl (2009).

Sr–Nd Isotopic Analysis

The Sr and Nd isotopic analytical work was performed at the Department of Lithospheric Research (University of Vienna, Austria). Sixteen of the 41 aforementioned samples were selected, including granite ($n = 14$) and granite clasts ($n = 2$).

Rock powders (approximately 50–100 mg) were digested in tightly screwed Savillex beakers using an ultra-pure mixture of HF:HNO₃ (4:1 ratio) for 2–

4 weeks at 100–120 °C on a hot plate, in order to make sure the insoluble phases, such as zircon, were fully digested. After acid evaporation, repeated treatment of the residue using 6 M HCl resulted in clear solutions. Element isolation for Sr and rare earth elements (REE) was performed using AG 50W-X8 (200–400 mesh, Bio-Rad) resin and 2.5 and 4.0 M HCl as eluants. Neodymium was separated from the REE group using Teflon-coated HDEHP and 0.22 M HCl as eluant. Maximum total procedural blanks were <1 ng for Sr and 40 pg for Nd, which can be considered negligible for the purpose of this work. The isolated element fractions were loaded on an Re double filament assembly and run in static mode on a Thermo-Finnigan Triton thermal ionization mass spectrometer (TIMS) instrument. Mass fractionation was corrected for $^{88}\text{Sr}/^{86}\text{Sr} = 8.3752$ and $^{146}\text{Nd}/^{144}\text{Nd} = 0.7219$, respectively. Samples were measured in two successive batches. Mean $^{87}\text{Sr}/^{86}\text{Sr}$ of 0.710260 ± 0.000004 (batch 1, $n = 5$) and 0.710257 ± 0.000006 (batch 2, $n = 5$) were determined for the NBS987 (Sr) and mean $^{143}\text{Nd}/^{144}\text{Nd}$ ratios of 0.511846 ± 0.000003 (batch 1, $n = 5$) and 0.511841 ± 0.000002 (batch 2, $n = 5$) for the La Jolla (Nd) international standards during the period of investigation. Uncertainties quoted represent 2σ errors of the mean. The isotopic ratios $^{87}\text{Rb}/^{86}\text{Sr}$ and $^{147}\text{Sm}/^{144}\text{Nd}$ were derived from Rb/Sr and Sm/Nd ratios obtained following Rb–Sr and Sm–Nd concentration measurements performed by XRF and INAA, respectively. The assigned uncertainties to $^{87}\text{Rb}/^{86}\text{Sr}$ and $^{147}\text{Sm}/^{144}\text{Nd}$ are 1 and 7%, respectively, with an uncertainty on Rb, Sr, Sm, and Nd measurements of 1, 0.4, 2, and 5%, respectively (Son and Koeberl 2005; Mader and Koeberl 2009; Nagl and Mader 2019).

RESULTS

Petrography

Granites and Granite Clasts

The investigated samples mainly consist of equigranular coarse-grained, holocrystalline and phaneritic leucogranite. The bulk mineral assemblage is mainly composed of orange to brownish K-feldspar (orthoclase, ~25–50 vol%); plagioclase (~15–35 vol%); quartz (~15–35 vol%); and, to a lesser extent, biotite (generally 1–5 vol%). Two samples (156R3_11–15 and 272R1_28–30.5) display a higher biotite content of ~10 vol%. The grain size varies from ~0.5 to 4 cm for K-feldspar, plagioclase, and quartz, and from ~0.1 to 1 cm for biotite (Figs. 3 and 4). Textural and compositional variations are common throughout the

granite unit. The main accessory minerals are muscovite, (fluor)apatite, titanite, secondary epidote (piemontite) located in cataclasite areas or associated with calcite veins, zircon, (titano)magnetite, and allanite. Other accessory minerals, including monazite, ilmenite, rutile, chalcopyrite, cobaltoan pyrite, stolzite/raspite, galena, uranothorite, and uranothorianite, were also detected during an SEM survey (Fig. 5). These accessory phases represent <1 vol% of the mineral assemblage and grain size is never more than 0.5 mm. Alteration is pervasive, as evidenced by epidote mineralization; sericitization of plagioclases; common chloritization of biotite; and the presence, to some extent, of secondary albite/K-feldspar veins crosscutting the granite unit (Fig. 4) (see also Kring et al. 2020). Granite alteration appears to be more pronounced in close proximity to impact melt rock dikes and along fractures.

The granite unit is pervasively deformed to different degrees from one sample to another, ranging from not or slightly deformed to displaying strong mineral deformation associated with foliation, this ductile deformation is thought to be pre-impact, providing evidence for local shear zones cutting the granite (see Fig. 3B). In addition, fracturing and shearing that occurred during the impact are abundant, as well as the presence of cataclasite veins made of microbrecciated material (mainly submillimeter-sized feldspars and quartz grains, as well as calcite) cross-cutting the granite (from millimeter to several centimeters in thickness, see Figs. 3C, 3D, and 4). In some cases, the cataclasites exhibit a greenish color associated with the presence of secondary epidote (piemontite), likely due to hydrothermal alteration (Kring et al. 2020). Postimpact calcite veinlets commonly cut through the granite samples. These veinlets are clearly indicated by μXRF mapping (Fig. 6). In addition, calcite fillings are observed in some planar fractures (PFs) within quartz grains (see also Ferrière et al. 2017; Feignon et al. 2020).

Impact-induced shock metamorphic features are apparent in most rock-forming minerals, that is, multiple sets of PFs, feather features (FFs), in average 2.8 sets of planar deformation features (PDFs), undulose extinction, and occasional kinkbanding in quartz grains (for details, see Feignon et al. 2020); in alkali-feldspar and plagioclase (i.e., PFs filled with opaque minerals and also some possible PDFs; see Pittarello et al. 2020), titanite, and apatite (with different types of planar microstructures; Timms et al. 2019; Cox et al. 2020). Kinkbanding is common in biotite, muscovite, and chlorite and also observed, to a lesser extent, in plagioclase and in quartz (Figs. 4D–F).

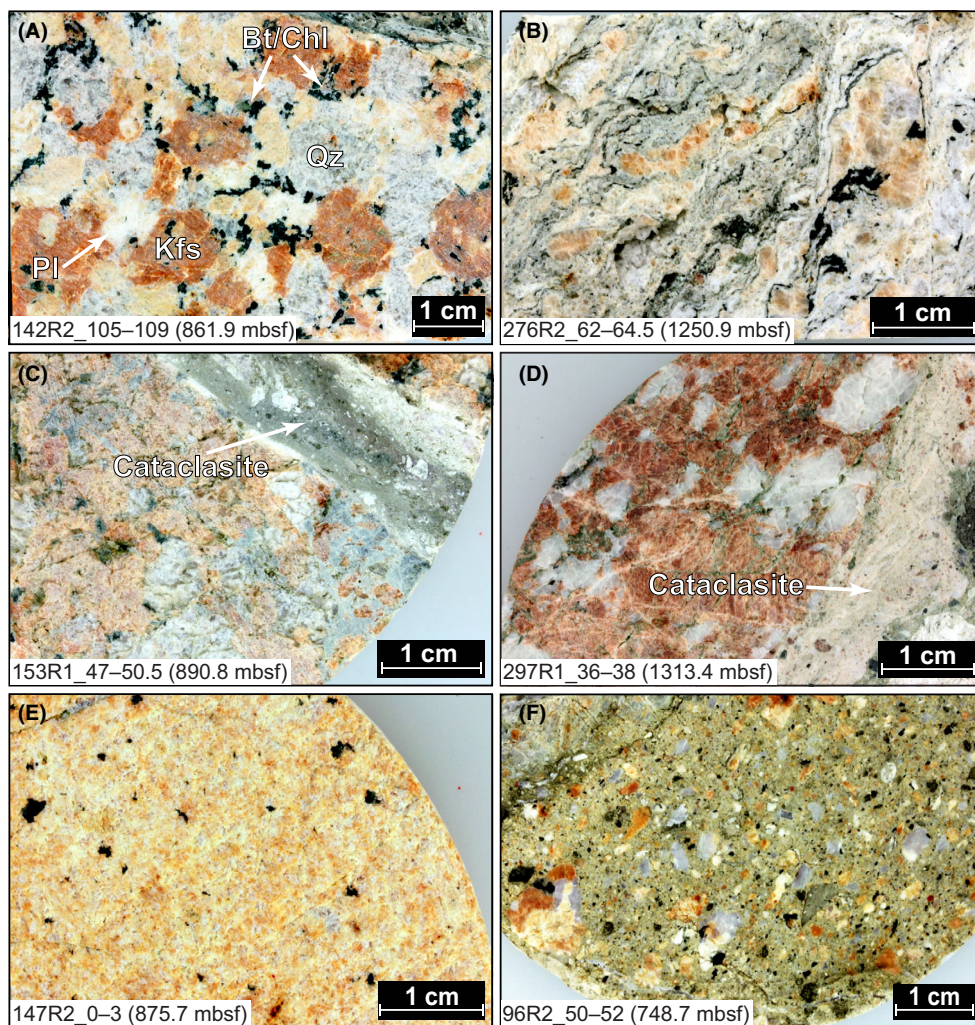


Fig. 3. Macrophotographs of the different sample types from the “lower peak ring” section of the Hole M0077A core investigated in this study. A) Coarse-grained granite, relatively undeformed with limited fracturing, exhibiting the typical paragenesis: K-feldspar (Kfs), quartz (Qz), plagioclase (Pl), biotite (Bt), and chlorite (Chl). B) Highly deformed granite sample with foliated minerals. C and D) Granite samples cross-cut by centimeter-sized cataclasite veins made up of microbrecciated material. The alteration is occurring mainly at the contact between the granite and cataclasite in (D), with greenish mineralization. E) Typical aplite sample with a fine-grained mineralogy and a low-biotite content. F) One of the two investigated granite breccia samples comprises a greenish-gray matrix with mainly K-feldspar and quartz as mineral clasts. (Color figure can be viewed at wileyonlinelibrary.com.)

Granite Breccias

Two of the investigated samples consist of monomict granite breccia. The upper sample (96R2_50–52, 748.7 mbsf) is made of subrounded, ~0.5 mm mineral clasts (mainly quartz and K-feldspar) with rare occurrence (<2 vol%) of biotite (Figs. 3F and 6E). The matrix (~45 vol%) is made of brecciated quartz; K-feldspar; and, to a lesser extent, calcite. The clastic breccia shows no signs of melting.

The second sample (278R1_43–45, 1256.0 mbsf) is similarly brecciated (with ~50 vol% of matrix), but more strongly deformed than 96R2_50–52, with a clear

mylonitic-like texture. In addition, the breccia is in contact with a large, 7 cm sized, coarse-grained granite.

Aplites

Samples 147R2_0–3 and 242R3_23–26 (875.7 and 1149.0 mbsf, respectively) are aplites with a fine-grained (average mineral size is <1 mm), homogeneous, equigranular texture (Fig. 3E). The main mineral phases are K-feldspar, quartz, and plagioclase whereas biotite is nearly absent (<1 vol%). Plagioclase exhibits sericitization and some calcite veins crosscut the samples. Shock features in the form of PFs and up to

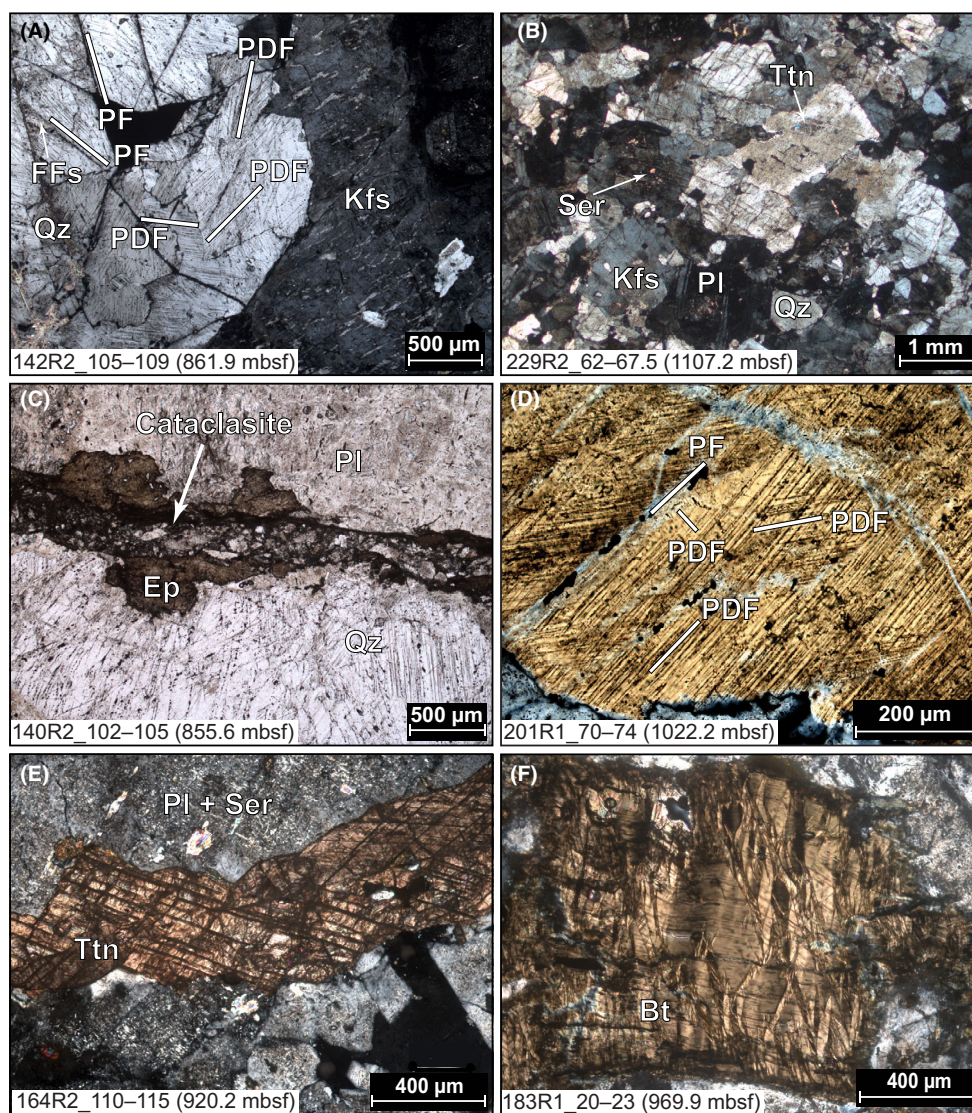


Fig. 4. Thin section photomicrographs (all in cross-polarized light except C in natural transmitted light). A) Typical granite sample with K-feldspar (Kfs) and quartz (Qz) crystals. Quartz is shocked with at least two sets of PF (with FFs) and several sets of PDF, not all shown for image clarity. No obvious shock features are visible on the K-feldspar in this case. B) Granite sample with a finer mean grain size, near aplitic texture. Plagioclase (Pl) is sericitized. Ttn = titanite. C) Cataclasite vein, characterized by brecciated quartz and feldspars, crossing the field of view. Epidote crystals (Ep, piemontite) are localized at the contact between cataclasite and the host rock (i.e., in this case mainly quartz and feldspars). D) Shocked quartz grain with two prominent decorated PDF sets. A third set of PDFs and a set of PFs, barely visible on this photograph, are also indicated with white marks. E) A titanite crystal with well-developed shock-induced planar microstructures (at least two sets visible) next to a sericitized (Ser) plagioclase. F) Large well-developed kinkbands in biotite (Bt). (Color figure can be viewed at wileyonlinelibrary.com.)

three sets of PDFs are observed in quartz grains, while shock microstructures are in some cases also observed in plagioclase.

Geochemistry

Major element contents of all investigated granitoid samples are presented in Table 1 and averaged trace element compositions for each type of sample (i.e.,

granite from the main unit, granite clast, granite breccia, and aplite) are presented in Table 2. Trace element compositions for all 41 investigated samples are reported in Data S1 in supporting information. Strontium and Nd isotopic data are reported in Table 3. In order to allow a discussion of the geochemical patterns of the investigated samples, the contents of selected major (SiO_2 , Al_2O_3 , CaO , and K_2O) and trace (Ba, Sr, Zr) elements, $^{87}\text{Sr}/^{86}\text{Sr}$ and $(\epsilon_{\text{Nd}})_{t=0}$

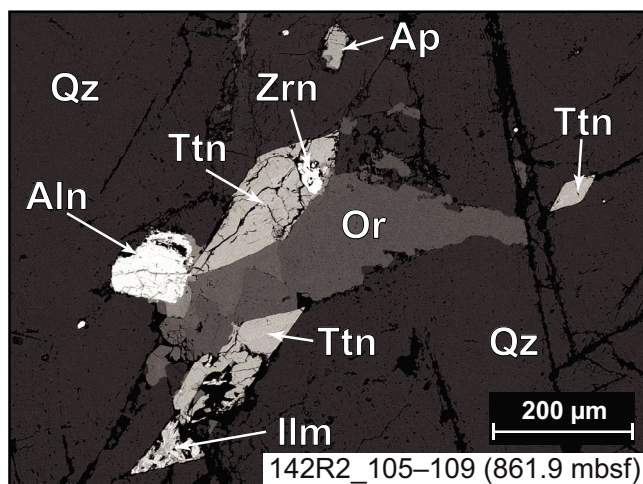


Fig. 5. SEM backscattered electron (BSE) image of an assemblage of the most commonly encountered accessory minerals in the investigated granite samples. Qz = quartz; Or = orthoclase; Ttn = titanite; Ap = apatite; Zrn = zircon; Aln = allanite; Ilm = ilmenite. (Color figure can be viewed at wileyonlinelibrary.com.)

have been plotted against depth from 745.1 to 1333.7 mbsf (Fig. 2). The LOI recorded for all the samples is relatively low (<2.6%, average of $0.91 \pm 0.55\%$, $n = 41$); thus, the data were not recalculated on an LOI-free basis, as this would not change the major element contents significantly. Interestingly, the highest LOI values (>1.5%) are observed for samples located in proximity (<0.5 m) of fractures, shearing areas, and/or dikes (both pre- and postimpact in origin), supporting more pronounced granite alteration near these features, as observed in the petrographic investigations.

Major Elements

Major elements show broadly similar patterns with few exceptions (see Fig. 7), independently of the sample type (granite, granite clast, granite breccia, or aplite) or

the depth in the drill core (Fig. 2), and represent the most evolved lithology compared to pre-impact dikes, suevites, and impact melt rocks (Morgan et al. 2017). Nearly all the samples show a granitic composition, with the SiO_2 and total alkali ($\text{Na}_2\text{O} + \text{K}_2\text{O}$) contents ranging from 69.68 to 77.45 wt% and from 6.85 and 9.38 wt%, respectively. Two samples plot outside the granite field and display a monzo-granitic composition with 156R3_11–15 having the lowest SiO_2 content (66.66 wt%) and 8.97 wt% total alkalis, whereas 116R2_58–62 shows the highest total alkali content (9.63 wt%) and 69.73 wt% SiO_2 . The investigated granitoid sample suite spreads between the calc-alkaline and the high-K calc-alkaline series (Ewart 1982), with K_2O contents ranging from 2.27 to 5.16 wt%. The Al_2O_3 contents show a continuous, decreasing trend from 16.06 to 11.55 wt% and are accompanied by increasing SiO_2 concentrations. A less pronounced decreasing trend can be noticed for CaO concentration (0.70–3.04 wt%), while other major elements in the investigated samples do not show a clear trend with increasing SiO_2 concentrations but exhibit rather relatively low and homogeneous compositions with limited variations in the Fe_2O_3^* (0.55–2.55 wt%), TiO_2 (0.05–0.38 wt%), and MgO (0.07–1.32 wt%) contents, highlighting the evolved nature of these samples relative to the other lithologies present in the drill core (i.e., suevites, impact melt rocks, and pre-impact dikes, such as dolerite and dacite; see e.g., Morgan et al. 2017; de Graaff et al. 2021). Additionally, the very high SiO_2 contents of all granite samples characterized here indicate a higher degree of fractionation.

The main outlier is sample 156R3_11–15, the least evolved sample with a quartz-monzonite composition, having the highest contents in Fe_2O_3 (3.76 wt%), MgO (1.35 wt%), TiO_2 (0.48 wt%), and P_2O_5 (0.34 wt%) of the investigated sample suite. These relatively high contents can be explained petrographically, as this sample contains ~10% of biotite; additionally, apatite

Fig. 6. Micro-XRF overview of representative investigated granitoid samples thick sections. A) Multi-element (Fe–Si–Ca–K) maps of eight samples. The upper row displays four granites from the main unit, highlighting some of the textural differences. The granite sample 134R3_75–79 is in contact with a dolerite dike and crosscut by several calcite veins. A large cataclasite vein occurs in sample 153R1_47–50.5. Iron is more abundant at the contact between cataclasite and granite while the matrix is relatively enriched in K, thus dominated by brecciated K-feldspar; then quartz; and, to a lesser extent, calcite (Ca-rich area within the cataclasite). The lower row shows two granite clasts, one aplite, and one granite breccia samples. The bulk geochemistry of all these samples is fairly similar; however, the main differences are textural (i.e., deformation; alteration features; or, to a lesser extent, interaction with impact melt rock or dike). B) Strontium distribution map (heatmap) of the same samples shown in (A). The plus and minus on the color scale indicate a high or a low abundance of Sr, respectively. These eight granitoid samples were mapped simultaneously, resulting in a semiquantitative distribution of Sr. Strontium contents display variations from one sample to another. While it is mostly concentrated in plagioclase, a relatively higher Sr content is observed in the Ca-rich area of the cataclasite. The lower Sr content in granite clast 295R2_51–53 is also confirmed by INAA and isotopic analysis (Table 3). Scanned images of thick sections are available in Fig. S1 in supporting information. IMR = impact melt rock. (Color figure can be viewed at wileyonlinelibrary.com.)

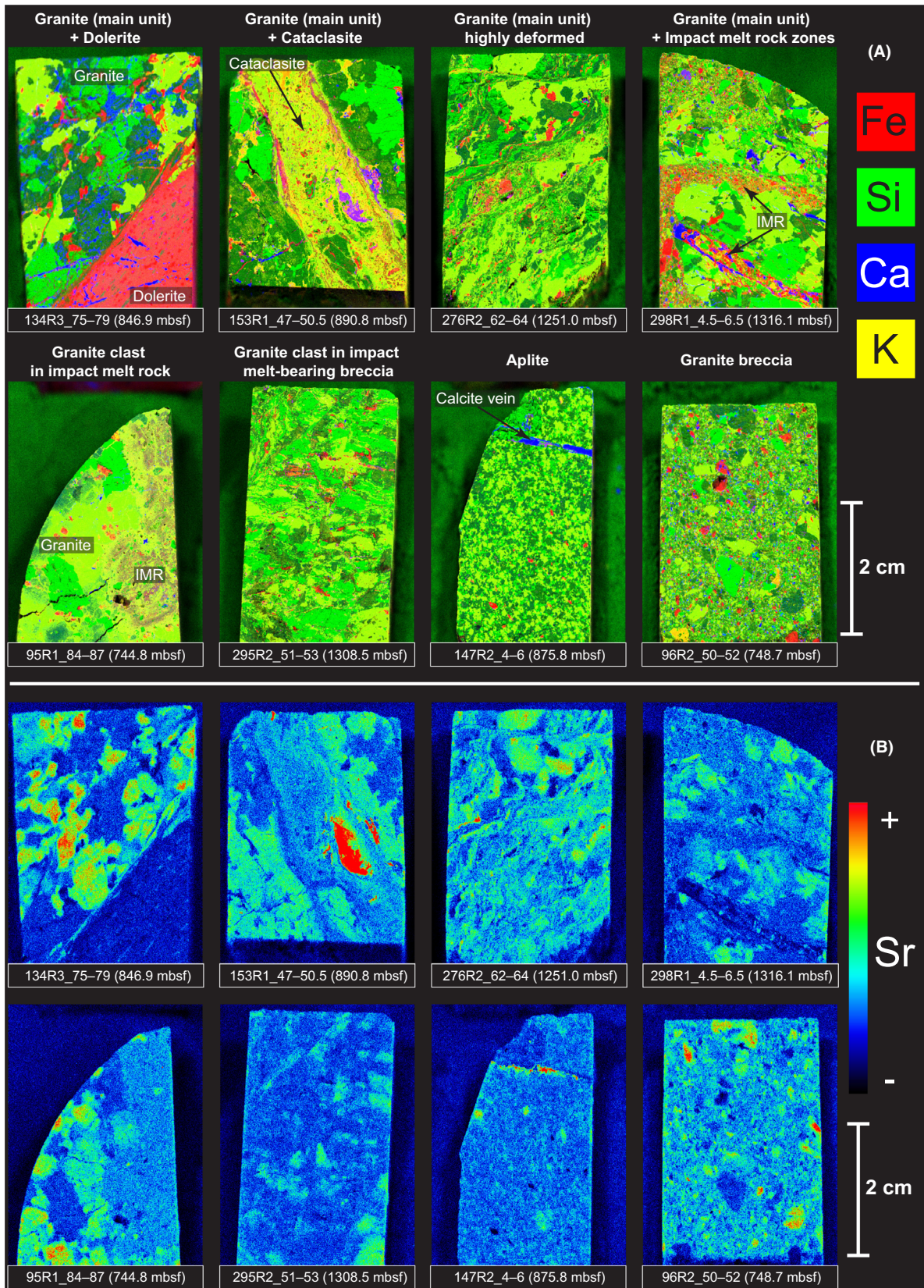


Table 2. Averages and range of trace element contents (all in ppm) for each of the investigated sample types from the Expedition 364 Chicxulub drill core (i.e., granites from the main unit, granite clasts, granite breccias, and aplites) as obtained using INAA and bulk XRF. Detailed results for each sample are available in Data S1.

	Granites ($n = 33$)		Granite clasts ($n = 4$)		Granite breccias ($n = 2$)		Aplites ($n = 2$)	
	Average	Range	Average	Range	Average	Range	Average	Range
Sc	3.07	1.57–7.82	3.20	2.72–4.06	4.16	3.84–4.49	2.72	1.98–3.46
V*	28.8	12.5–76.0	26.6	18.4–30.1	42.6	36.4–48.7	10.8	6.70–14.8
Cr	11.4	7.27–21.2	10.8	9.67–11.8	20.9	10.9–30.9	6.26	5.41–7.10
Co	3.33	1.22–10.1	3.45	1.91–6.45	4.52	3.42–5.62	0.72	0.52–0.92
Ni*	3.91	1.80–10.2	4.45	2.70–7.10	9.40	4.60–14.2	0.70	0.50–0.90
Cu*	18.4	8.40–123	13.1	9.90–19.0	17.1	12.2–21.9	13.8	11.0–16.5
Zn*	26.2	4.00–89.8	17.4	6.30–25.6	20.5	11.9–29.0	10.6	7.30–13.8
As*	1.50	b.d.l.–3.10	2.27	b.d.l.–4.60	2.20	1.40–3.00	1.75	1.70–1.80
Rb*	126	87.1–171	129	101–159	122	122–122	181	175–187
Ba*	468	229–847	391	211–532	343	266–420	176	170–182
Th*	11.4	5.20–20.0	15.3	8.90–26.3	11.4	9.70–13.1	15.1	13.6–16.5
U*	7.50	3.80–30.2	6.20	2.90–9.20	6.10	5.20–7.00	8.10	5.30–10.9
Nb*	6.49	3.20–12.2	6.13	5.50–7.00	7.05	5.60–8.50	12.5	11.8–13.2
Ta	0.60	0.30–0.95	0.59	0.46–0.76	0.65	0.52–0.79	1.55	1.14–1.97
La	15.0	2.10–30.5	11.3	4.60–14.4	16.7	12.7–20.7	7.50	10.4–4.50
Ce	29.6	9.70–56.2	26.3	10.1–34.0	27.3	26.3–28.3	13.6	10.6–16.5
Pb*	25.3	13.4–98.5	22.6	17.5–33.3	152	24.1–280	32.7	26.2–39.2
Sr*	351	200–491	321	195–450	311	270–352	185	179–192
Nd	11.2	4.00–23.0	11.3	8.40–13.0	15.1	15.0–15.3	7.10	5.80–8.30
Zr*	103	69.2–204	94.9	78.4–117	110	97.3–123	52.7	52.6–52.8
Cs	1.51	0.75–4.87	1.18	0.57–1.50	1.19	1.10–1.30	1.52	1.38–1.67
Hf	3.08	2.03–5.91	2.74	2.42–3.38	3.51	3.06–3.97	2.74	2.63–2.86
Sm	2.38	1.09–5.96	2.39	1.74–3.10	2.80	2.54–3.10	2.48	2.66–2.29
Eu	0.45	0.27–0.85	0.46	0.34–0.60	0.53	0.46–0.60	0.40	0.40–0.40
Gd	2.03	1.03–4.56	1.87	1.24–2.52	1.96	1.32–2.60	2.00	1.54–2.46
Tb	0.16	0.10–0.36	0.16	0.13–0.20	0.21	0.19–0.20	0.23	0.20–0.26
Yb	0.60	0.23–1.04	0.55	0.35–0.70	0.62	0.48–0.76	0.75	0.61–0.90
Y*	5.97	3.70–10.9	6.45	5.60–7.50	8.05	6.80–9.30	7.20	6.20–8.20
Lu	0.08	0.05–0.14	0.09	0.06–0.10	0.11	0.08–0.14	0.10	0.10–0.10
K/Rb	256	158–319	282	250–332	249	234–264	193	192–194
Sr/Y	62.2	36.6–123	49.8	29.6–59.9	40.4	29.0–51.8	26.4	21.8–30.9
(La/Yb) _N	19.0	2.85–40.9	15.8	4.64–25.9	20.3	11.3–29.4	7.50	3.40–11.6

b.d.l. = below detection limit.

*Measured with XRF.

and titanite grains are also relatively more abundant than in the other investigated samples.

The relatively high CaO content (2.09–3.04 wt%) observed in four granite and in one granite breccia samples can be explained by (1) the presence of calcite-filled fractures, evidenced by the μ XRF mapping of sample 134R3_75–79 (Fig. 6A), the sample with the highest measured CaO contents (3.04 wt%), and the significant presence of calcite in the matrix of the granite breccia sample (see Fig. 6A), respectively, and/or (2) a higher proportion of plagioclase as is the case for sample 156R3_11–15, which displays ~35 vol% plagioclase and a lower abundance of calcite veins relative to the other CaO-rich granites.

Based on the $\text{Al}_2\text{O}_3/(\text{Na}_2\text{O} + \text{K}_2\text{O})$ versus $\text{Al}_2\text{O}_3/(\text{CaO} + \text{Na}_2\text{O} + \text{K}_2\text{O})$ diagram (see Fig. 10), the

investigated samples are metaluminous to weakly peraluminous. The $\text{K}_2\text{O}/\text{Na}_2\text{O}$ ratios of the granitoids range from 0.42 to 1.30, with an average of 0.84 ± 0.21 .

Trace Elements

Concerning trace element contents presented in CI-chondrite-normalized diagrams (Fig. 8), with normalization values from McDonough and Sun (1995), the granites from the main unit (Fig. 8A) show similar patterns to one another and to literature data (Zhao et al. 2020; de Graaff et al. 2021), with enriched compositions relative to CI-chondritic values. Fluid-mobile elements, such as Ba and U, are highly enriched, with samples 298R1_41–43 and 300R1_78–79.5, located in the lower part of the basement (1316.5 and 1323.1 mbsf, respectively), and highly fractured,

Table 3. Rb–Sr and Sm–Nd isotopic compositions of 14 granites and two granite clasts from the Expedition 364 Chicxulub drill core.

Sample	Depth (mbsf)	Rb (ppm)	Sr (ppm)	$^{87}\text{Rb}/^{86}\text{Sr}^{\text{a}}$	$^{87}\text{Sr}/^{86}\text{Sr}^{\text{b}}$	$^{87}\text{Sr}/^{86}\text{Sr}^{\text{b}}$	$^{87}\text{Sr}/^{86}\text{Sr}$ ($t=326\text{Ma}$)	Sm (ppm)	Nd (ppm)	$^{147}\text{Sm}/^{144}\text{Nd}^{\text{a}}$	$^{143}\text{Nd}/^{144}\text{Nd}^{\text{a}}$	$^{143}\text{Nd}/^{144}\text{Nd}^{\text{c}}$	$\epsilon_{\text{Nd}}^{\text{d}}$	$(\epsilon_{\text{Nd}})_{t=326\text{Ma}}$	$T_{\text{DM}}^{\text{Nd}}$ (^{326}Ma) (Ga) ^e
Granites															
97R3_10–12.5	752.5	143	333	1.2431	0.709614	0.70385	1.73	10.0	0.1025	0.512410	0.512410	0.512410	–4.4	–0.5	1.1
125R1_40–42.5	826.7	132	374	1.0217	0.708963	0.70422	1.70	8.03	0.1285	0.512470	0.512470	0.512470	–3.3	–0.4	1.1
136R2_20–25	851.4	114	447	0.7382	0.707975	0.70455	1.09	4.10	0.1607	0.512484	0.512484	0.512484	–3.0	–1.5	1.2
142R3_48–50	862.6	124	384	0.9347	0.708807	0.70447	4.09	23.0	0.1075	0.512424	0.512424	0.512424	–4.2	–0.5	1.1
153R1_47–50.5	890.8	125	269	1.3452	0.709801	0.70356	2.00	10.0	0.1209	0.512449	0.512449	0.512449	–3.7	–0.5	1.2
156R3_11–15	902.1	171	404	1.2254	0.710231	0.70454	1.20	19.0	0.0382	0.512464	0.512464	0.512464	–3.4	3.2	0.8
176R2_112–116	953.6	159	231	1.9933	0.713210	0.70396	1.94	14.0	0.0838	0.512433	0.512433	0.512433	–4.0	0.7	1.0
200R3_12.5–15	1021.0	109	368	0.8573	0.708447	0.70447	2.47	13.9	0.1074	0.512439	0.512439	0.512439	–3.9	–0.2	1.1
229R2_62–67	1107.2	89	319	0.8075	0.708159	0.70441	2.02	14.0	0.0872	0.512467	0.512467	0.512467	–3.3	1.2	0.9
266R2_95.5–98.5	1220.5	106	444	0.6910	0.707981	0.70477	2.16	16.0	0.0816	0.512436	0.512436	0.512436	–3.9	0.8	1.0
280R2_51.5–53.5	1263.5	163	220	2.1457	0.713705	0.70375	2.80	10.4	0.1628	0.512477	0.512477	0.512477	–3.1	–1.7	1.2
297R1_36–38	1313.4	167	265	1.8248	0.712105	0.70364	1.36	4.00	0.2055	0.512454	0.512454	0.512454	–3.6	–4.0	1.4
299R1_52.5–55.5	1319.7	118	200	1.7083	0.711652	0.70373	1.39	9.00	0.0934	0.512447	0.512447	0.512447	–3.7	0.6	1.0
300R1_78–79.5	1323.1	162	291	1.6118	0.711322	0.70384	3.25	11.8	0.1659	0.512449	0.512449	0.512449	–3.7	–2.4	1.2
Granite clasts															
285R2_26–28.5	1278.7	113	317	1.0319	0.709111	0.70432	3.10	12.6	0.1487	0.512447	0.512447	0.512447	–3.7	–1.7	1.2
295R2_51–53	1308.5	159	195	2.3614	0.713686	0.70273	1.82	13.0	0.0846	0.512440	0.512440	0.512440	–3.9	0.8	1.0

^aUncertainties on $^{87}\text{Rb}/^{86}\text{Sr}$ and $^{147}\text{Sm}/^{144}\text{Nd}$ are $\pm 1.0\%$ and $\pm 5.0\%$, respectively.

^bThe uncertainty on $^{87}\text{Sr}/^{86}\text{Sr}$ ratio is $\pm 2\sigma = 0.000004$.

^cThe uncertainty on $^{143}\text{Nd}/^{144}\text{Nd}$ ratio is $\pm 2\sigma = 0.000004$.

^dCalculated using $^{143}\text{Nd}/^{144}\text{Nd}_{\text{CHUR}} = 0.512638$ (DePaolo and Wasserburg 1976). CHUR = chondritic uniform reservoir.

^eTwo-stage Nd model age calculated following the method of Liew and Hofmann (1988) with $^{143}\text{Nd}/^{144}\text{Nd}_{\text{DM}} = 0.513151$, $^{147}\text{Sm}/^{144}\text{Nd}_{\text{DM}} = 0.219$, and $^{147}\text{Sm}/^{144}\text{Nd}_{\text{CC}} = 0.12$. DM = depleted mantle; CC = continental crust.

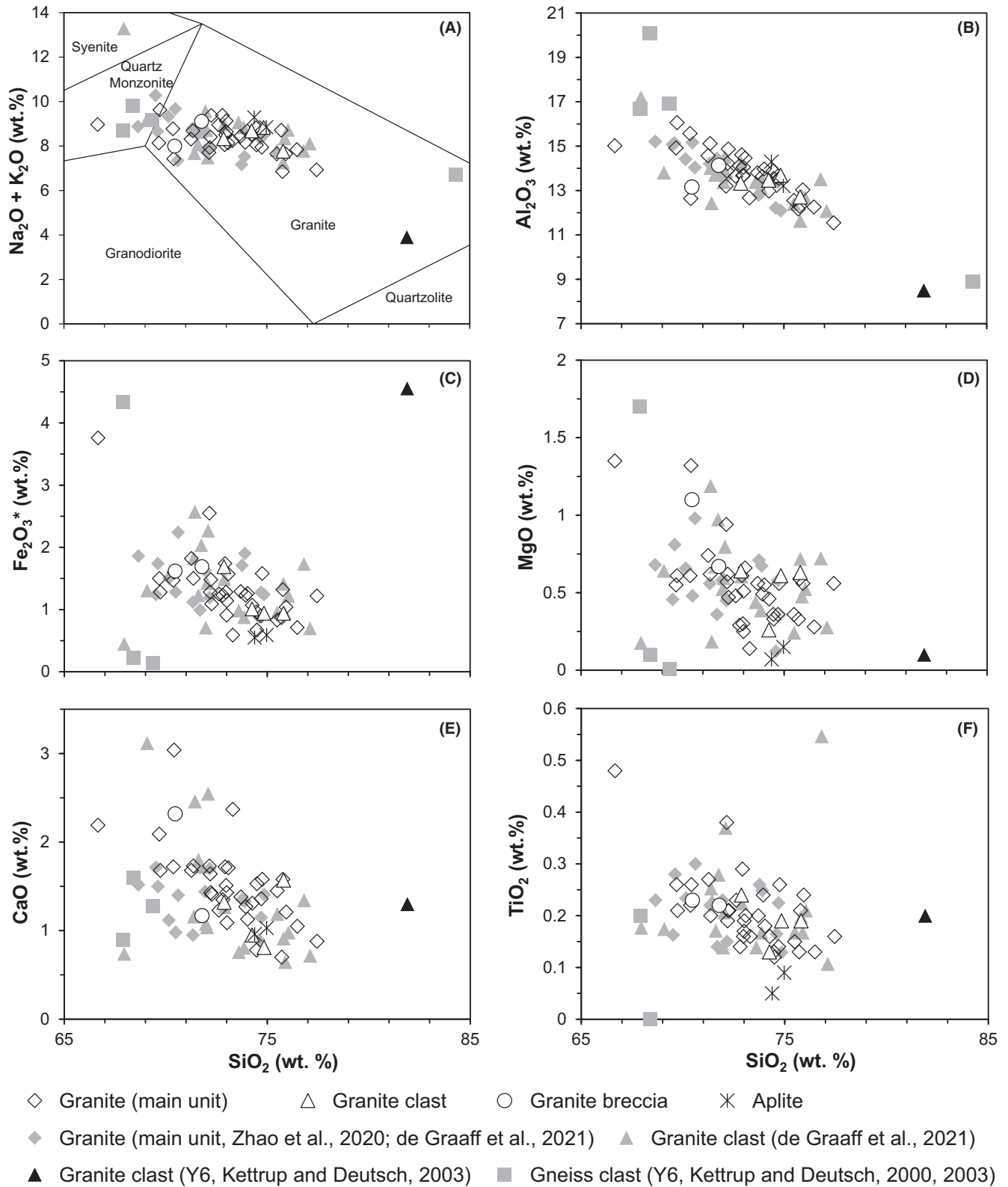


Fig. 7. A) Total alkalis versus SiO_2 (TAS) diagram (upper left) modified from Middlemost (1994). B–F) Harker diagrams of Al_2O_3 , Fe_2O_3^* (total ferrous Fe), MgO, CaO, and TiO_2 versus SiO_2 for the investigated granite, granite clast, granite breccia, and aplite samples.

showing values more than 1000 times the CI-chondritic value for U, whereas a depletion of Pb is observed for nearly all the samples. In contrast, Nb and Ta show a relative depletion, while Zr and Hf show a moderate enrichment, relative to neighboring trace elements, a pattern typical of arc-type magmatism (Pearce et al. 1984). Otherwise, the granites are mainly characterized by light rare earth elements (LREE) with concentrations higher than 10 times CI-chondritic values and lower contents of heavy rare earth elements (HREE), below 10 times the CI-chondritic values, and displaying a relatively flat pattern. No pronounced positive or negative Eu anomalies were recorded. Additionally, Yb shows a slight negative anomaly relative to Er and Y (Yb^* is 0.81 ± 0.30 , $Yb^* = Yb_N/[Er_N \times Y_N]^{0.5}$, $n = 33$) in some of the samples. While similar Yb negative anomalies may previously have been observed, Yb is more slightly depleted relative to Lu in the samples investigated by Zhao et al. (2020) and de Graaff et al. (2021), and thus, an analytical artifact cannot be fully excluded here. Negative Yb anomalies require highly reducing conditions to occur and are typically coupled with clear Eu anomalies (Hsu 2003), which are not observed in our samples. Finally, some samples show either a depletion or an enrichment in some elements relative to the large majority of the granites. Sample 136R2_20–25 is depleted in La and Nd (an Nd depletion is also observed for 297R1_36–38), whereas sample 153R1_47–50.5 exhibits no depletion in Pb compared to the other investigated samples.

The trace element compositions of the granite clasts are plotted in Fig. 8B. The concentrations for the plotted elements are within the range of the investigated granite samples from the main unit, with only sample 95R2_19–22 showing a small depletion in La and Ce and an enriched Sr composition compared to the other clasts investigated.

The trace element contents of the two investigated granite breccia samples are shown in Fig. 8C. Sample 278R1_43–45 does not exhibit any significant differences compared to the main granite suite, whereas sample 96R2_50–52 shows a clear enrichment in Pb (280 ppm relative to the <99 ppm in the main granite group), which may be explained by the presence of a Pb-bearing phase (e.g., sulfide minerals). These secondary phases are commonly observed in the impact melt-bearing breccias (see Kring et al. 2020), making this Pb-enrichment secondary. The Pb composition of this specific sample (as for granite 153R1_47–50.5) is similar to that of the “upper impact melt rock” sample 100_2_89.5_91.5 investigated by de Graaff et al. (2021) and may have a similar secondary Pb-enriched component.

The two investigated aplites (Fig. 8D) have trace element composition patterns somewhat similar to those of the granites, with only a slight enrichment in Ta and a depletion in Ba and Zr concentrations. Sample 147R2_0–3 is also slightly depleted in La concentrations compared to the granites. However, in bivariate immobile trace element diagrams (Fig. 9), the aplites plot slightly outside of the main trend as defined by the granites; the difference is even more striking in the Ta versus Nb diagram (Fig. 9B).

Sr–Nd Isotopic Ratios

In the 16 investigated granite samples (including two granite clasts from the lower part of the core; samples 285R2_26–28.5 and 295R2_51–53), the element concentrations range from 89 to 171 ppm Rb, 195 to 447 ppm Sr, 1.1 to 4.1 ppm Sm, and 4.1 to 23 ppm Nd. The granite clasts do not have distinct Rb–Sr/Nd–Sm concentrations relative to the main granite group (Table 3). The Rb/Sr and Sm/Nd ratios vary from 0.24 to 0.82 and from 0.14 to 0.27, respectively. Only granite 156R3_11–15 shows a lower Sm/Nd ratio of 0.06.

The present-day $^{87}\text{Sr}/^{86}\text{Sr}$ ratios show a clear variability, ranging from 0.70798 and 0.71371 (Table 3). Interestingly, the samples located close to the bulk of the LIMB, in the lower part of the granite unit (at 1263.5 mbsf, $n = 6$), where several impact melt rock and suevite dikes occur, and where the granite exhibits higher degrees of deformation relative to the upper samples, generally display more radiogenic compositions than in the upper part ($n = 10$), with average $^{87}\text{Sr}/^{86}\text{Sr}$ of 0.711930 and 0.709319, respectively. Only sample 176R2_112–116 (953.6 mbsf) has a distinct, more radiogenic composition in the upper part of the granite unit, with an $^{87}\text{Sr}/^{86}\text{Sr}$ of 0.713210. This particular sample is characterized by the presence of 2–3 mm cataclases and is near a contact with a 10 cm thick, pervasive, shear zone. The $^{87}\text{Rb}/^{86}\text{Sr}$ ratios range from 0.6910 to 2.3614. Samples in close proximity to the LIMB display a generally higher $^{87}\text{Rb}/^{86}\text{Sr}$ ratio (average of 1.7807) compared to the samples located in the upper part of the granite unit (average of 1.0857). The investigated samples form an isochron between $^{87}\text{Sr}/^{86}\text{Sr}$ and $^{87}\text{Rb}/^{86}\text{Sr}$ (see Fig. 11C). Given the estimated errors on the $^{87}\text{Sr}/^{86}\text{Sr}$ and $^{87}\text{Rb}/^{86}\text{Sr}$ ratios, the isochron has a very high scattering with a mean square of weighed deviates (MSWD) of 25. The MSWD of the isochron is well above the value for a statistically acceptable isochron, defined at <~2.5 by Brooks et al. (1972), and, thus, should be considered to represent an errorchron, indicating that the Rb–Sr system has not been completely reset. The apparent regression age is calculated to be 273 ± 21 Ma, with an initial $^{87}\text{Sr}/^{86}\text{Sr}$

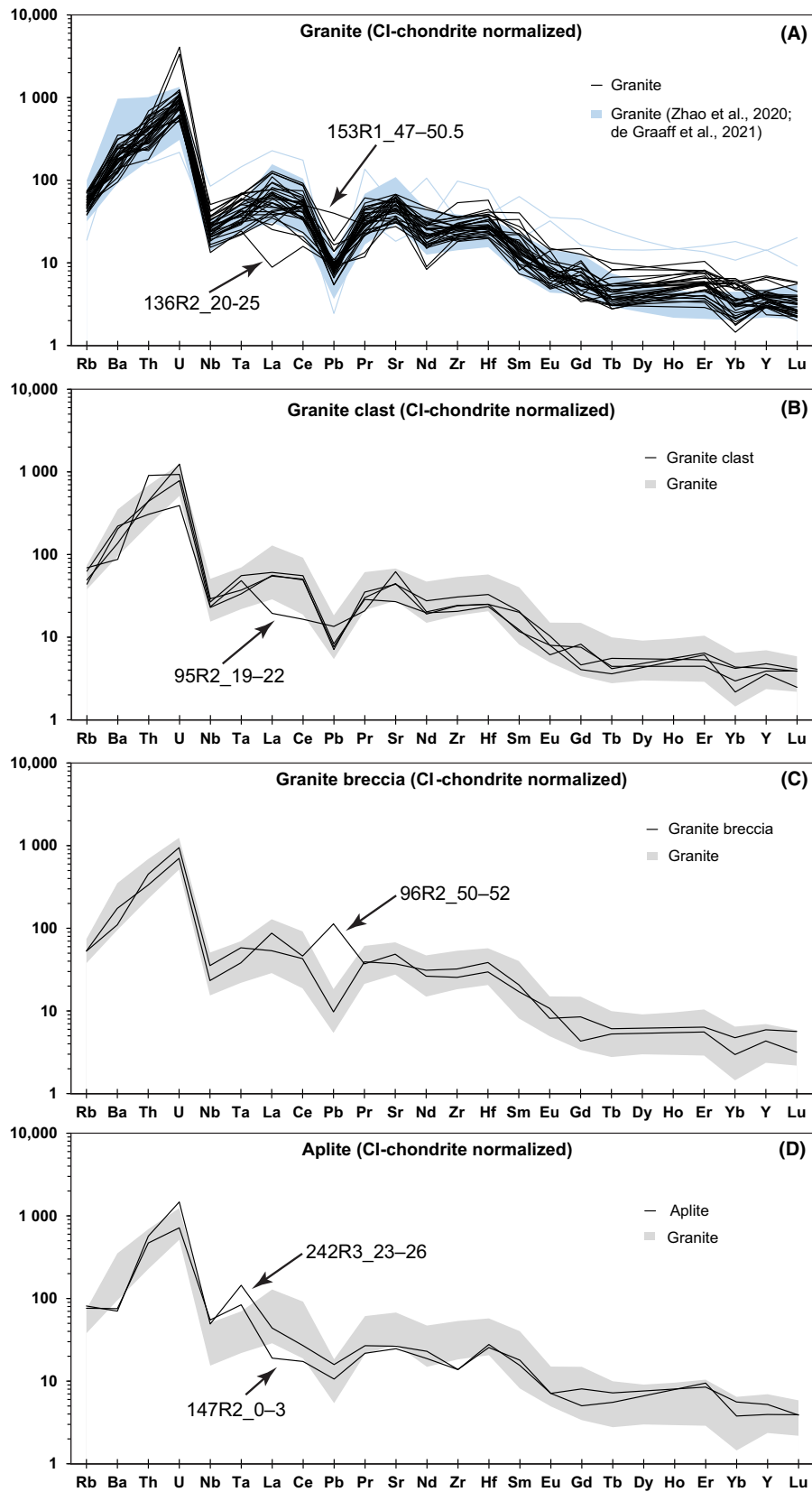


Fig. 8. A–D) CI-chondrite-normalized trace element compositions, with normalization values from McDonough and Sun (1995). A) The blue area in the upper diagram represents the compositions from previous work made on granite from the M0077A core (Zhao et al. 2020; de Graaff et al. 2021). B–D) The gray outline represents the main composition of all the granite samples investigated in this study, to allow a comparison with the granite clast, breccia, and aplite samples. Investigated samples have highly similar patterns, except one granite breccia with a significant Pb positive anomaly that may due to the presence of a Pb-bearing phase. (Color figure can be viewed at wileyonlinelibrary.com.)

of 0.705164 ± 0.0003 . However, given the high uncertainty on age determination and its deviation from the well-constrained U–Pb Carboniferous ages obtained in zircons by Zhao et al. (2020) and Ross et al. (2021), this apparent age obtained from the errorchron corresponds to a disturbance of the Rb–Sr system (see the Discussion section).

In contrast, current $^{143}\text{Nd}/^{144}\text{Nd}$ ratios display limited variations (0.512410–0.512484) and $(\epsilon_{\text{Nd}})_{t=0}$ values plot in a narrow range between -4.4 and -3.0 for all the investigated samples. The corresponding $^{147}\text{Sm}/^{144}\text{Nd}$ ratios vary from 0.0816 to 0.2055, while granite sample 156R3_11–15 shows a lower $^{147}\text{Sm}/^{144}\text{Nd}$ ratio of 0.0382 (Table 3). There is no significant difference observed between samples in the upper part of the granite unit and the samples in the lower part, next to the LIMB, indicating that Nd remained mostly unaffected by alteration processes.

Based on the work of Zhao et al. (2020), the initial $^{87}\text{Sr}/^{86}\text{Sr}$ and ϵ_{Nd} are calculated using $t = 326$ Ma. Initial $(^{87}\text{Sr}/^{86}\text{Sr})_{t=326\text{Ma}}$ are 0.70273–0.70477, while $(\epsilon_{\text{Nd}})_{t=326\text{Ma}}$ vary from -4.0 to 3.2 (see Fig. 11A). The Nd two-stage model age (DePaolo 1981; Liew and Hofmann 1988) $T_{\text{DM2}(326\text{Ma})}$ ranges between 0.8 and 1.4 Ga. The model ages are relatively similar for all samples (Table 3).

DISCUSSION

Granite Characterization

In general, the granitoids investigated in this study (i.e., granites, granite clasts, brecciated granites, and aplites) are relatively homogeneous in terms of their major element content (i.e., limited variations in composition or well-defined compositional trends). Only a single outlier compared to the other granitoids, the quartz-monzonite sample (156R3_11–15), with higher major element contents other than SiO_2 , as well as enrichments in Zr and Hf, is noted. The relatively high proportion of plagioclase (~35 vol%), biotite (~10 vol%), and zircon may explain the distinct chemical composition of this sample. No samples with clearly distinct compositions were identified, suggesting that the investigated granite clasts all belong to the main granite unit, and that the granite breccias did not experience

significant interaction with lithologies other than granite during their emplacement. Additionally, the textural variations (i.e., degree of deformation, presence of cataclastic veins) observed during petrographic investigations (see the Petrography section 4.1) within the main granite unit do not significantly affect the major element contents. As a result, for simplicity, all the investigated samples are from here onward termed “granite” (whether they are granite clasts or granite breccia samples; also including the aplite samples [except where indicated], which are a fine-grained equivalent of granite).

The granite samples are characterized by a decreasing Al_2O_3 and, to a lesser extent, CaO content, with increasing degrees of differentiation, as is commonly associated with fractionation of plagioclase (Langmuir et al. 1992; Sisson and Grove 1993), although the variation of modal mineral components (mainly the K-feldspar content relative to plagioclase) may contribute, to some extent, to these trends. However, the Al_2O_3 contents are relatively high, indicating a retention of plagioclase in the granite, albeit to a limited extent as no positive Eu anomaly is observed in any of the investigated samples. This observation further supports that the granites represent intrusions rather than cumulates (see also de Graaff et al. 2021). None of the samples investigated in this study display a distinct trace element composition that would either suggest interaction with other lithologies within the core (i.e., impact melt rock or pre-impact volcanic dikes) or a distinct granite type other than arc derived, implying that the granites sampled in the Hole M0077A core are related to a single magmatic intrusion event.

Our petrographic investigations and previous studies have highlighted the pervasive alteration of the recovered rocks from IODP-ICDP Expedition 364 drill core (Morgan et al. 2017; Simpson et al. 2020; de Graaff et al. 2021), following the onset of a long-living hydrothermal system (Kring et al. 2020) that could have affected the whole rock compositions, especially the mobile elements like Ba, Rb, and U. Immobile incompatible elements, especially high field strength elements (HFSE) like Zr, Hf, Nb, and Ta, are less affected by alteration processes, and can thus be used to trace the magmatic signatures of the granite samples

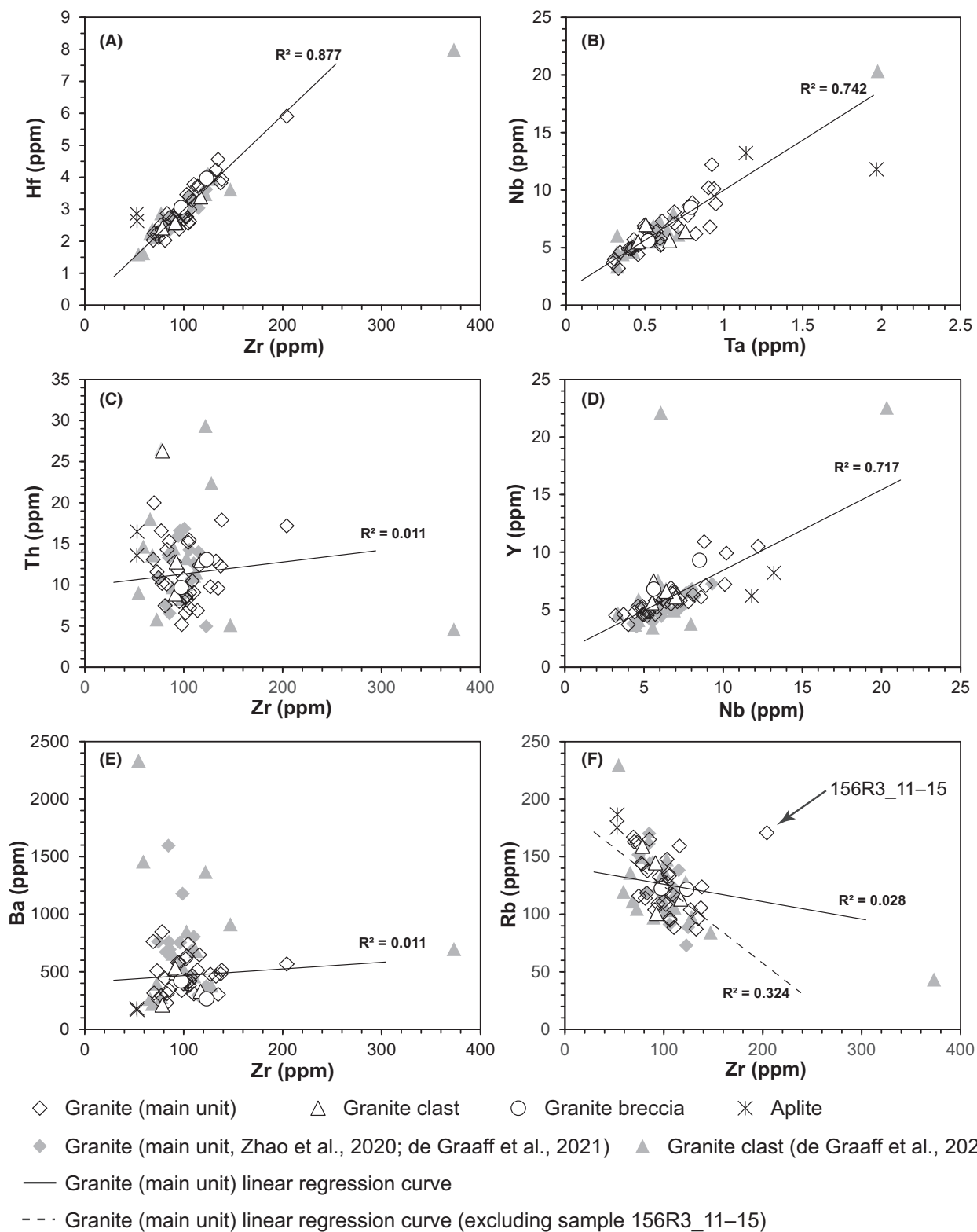


Fig. 9. A–F) Bivariate diagrams on trace element variations in granite samples. The trend line is calculated based on the main granite unit samples only. Zr versus Hf, Ta versus Nb, and Nb versus Y show strong covariations with R^2 above 0.7. The aplites plot slightly outside the main trend. Th, Ba, and Rb abundances are more scattered. In the Rb versus Zr diagram, the dashed trend line is calculated excluding the outlier samples enriched in Zr (i.e., sample 156R3_11–15) providing a better, although still low, covariation (R^2 of 0.324).

(e.g., Pearce et al. 1984; Pearce 2014). Strong linear covariations for all sample groups, with the notable exception of the aplite samples, which plot outside the main trend, are observed between Zr and Hf, Ta and Nb, and Nb and Y (Fig. 9). A similar linear correlation is observed when plotting Zr and V versus TiO₂ content (see Fig. S2 in supporting information). In contrast, Th, Ba, and U contents are more scattered when plotted versus Zr concentrations. A similar scattering is observed for Rb, but with a slightly lower importance than for Th, Ba, and U (Fig. 9 and Fig. S2). The decoupling between immobile and these mobile elements therefore indicates that they were probably affected by alteration. Additionally, as already shown in de Graaff et al. (2021), no covariation is observed between La and Zr (Fig. S2) in the granites investigated, with the (La/Yb)_N ratio displaying strong variation (from ~3 to ~41) while Yb_N has relatively similar contents. This observation confirms that La must have been remobilized by alteration processes within the Chicxulub impact structure (de Graaff et al. 2021).

In order to assess the degree of hydrothermal alteration of the investigated samples, the K/Rb ratio was used to discriminate between altered and less altered granites. According to Helvacı and Griffin (1983), less altered and unaltered crustal rocks show K/Rb ratio <300, while in the case of hydrothermally altered rocks, the K/Rb ratio is typically between 400 and 500. The average K/Rb ratio of the investigated samples is of 256 for the main granite group, 282 for the granite clasts, 249 for the granite breccias, and 193 for the aplites (Table 2). Four of the investigated samples exhibit K/Rb ratios slightly above 300, that is, granite clast 95R2_19–22 with a K/Rb of 332, and granite samples 110R2_14–16, 116R2_58–62, and 236R1_90–92.5 with K/Rb of 314, 306, and 319, respectively (Table 2). However, great care should be taken with the use of this ratio, as, on the one hand, Rb contents are decoupled relative to immobile elements like Zr, and on the other hand, postimpact K-metasomatism was clearly indicated throughout the Chicxulub impact structure and in the entire drill core (Hecht et al. 2004; Kring et al. 2020), and, thus, K/Rb and Na₂O/K₂O ratios may not totally reflect the original, primary magmatic signature of the Chicxulub granites.

As described in the Trace Elements section, the trace element contents of the granite indicate a typical arc-like signature characterized by Ta and Nb depletions (see also de Graaff et al. 2021) coupled with slight Lu (HREE) enrichment relative to HREE Yb, which is compatible with a source melted with garnet in the residue as also reported by Zhao et al. (2020) and de Graaff et al. (2021). Using the chemical classification

of Pearce et al. (1984) to decipher the tectonic context of the granite formation, the Rb content is plotted versus Y + Nb concentrations (Fig. 10B), as Rb and Nb are affected in a similar way by mantle heterogeneities, while Y remains unaffected. Even though some scattering of the data is noticed, all the samples plot within the volcanic arc granite field, close to or on the limit with the syn-collision granite array, which may suggest a transition between arc magmatism and a collisional context (Fig. 10B).

Interestingly, the two investigated aplite samples plot within the enriched-MORB array (Fig. 10C); together with their immobile element compositions (Fig. 9), this may suggest that the aplites were emplaced as dikes during a distinct event, with a more “enriched-MORB”-like source, or may result from a remelting of granite material (e.g., through local changes in the solidus temperature caused by fluid circulation or during a thermal event), or may be the result of a different crystallization stage of the granite. Further investigations are needed in order to confirm their origin.

The present-day more radiogenic ⁸⁷Sr/⁸⁶Sr and higher ⁸⁷Rb/⁸⁶Sr ratios are observed for samples in proximity to the LIMB (below 1263.5 mbsf), where the granites are generally highly deformed and crosscut by numerous, more or less thick, impact melt rock dikes, and for sample 176R2_112–116, recovered from a much shallower depth, at 953.6 mbsf, which is in contact with a 3–4 mm thick cataclasite. While these more radiogenic granites display slightly higher Rb contents (average 147 ppm) compared to the less radiogenic granites (average 127 ppm), they display a more pronounced depletion in Sr, with average concentrations of 357 and 258 ppm for the less radiogenic and the more radiogenic granites, respectively. These observations clearly indicate that the granite experienced hydrothermal alteration, affecting both Rb and Sr contents (as well as other mobile elements such as Ba, Th, and U), and that the impact-related features (i.e., impact melt rock dikes, cataclasites, shock-induced fractures at the mineral scale) may have enhanced the hydrothermal fluid circulation. The mobilization and slight enrichment in Rb (and also in other mobile trace elements) could be attributed to hydrothermal fluid alteration and/or to the supply of crustal material, while the Sr depletion could be related to the hydrothermal alteration of plagioclase, evidenced by the high level of sericitization occurring in plagioclases (Plimer and Elliott 1979; Cruciani et al. 2017).

However, fluid alteration by seawater alone cannot fully explain the present-day more radiogenic ⁸⁷Sr/⁸⁶Sr ratios measured, as the present-day ⁸⁷Sr/⁸⁶Sr of seawater is estimated at ~0.709 (Veizer 1989). Thus,

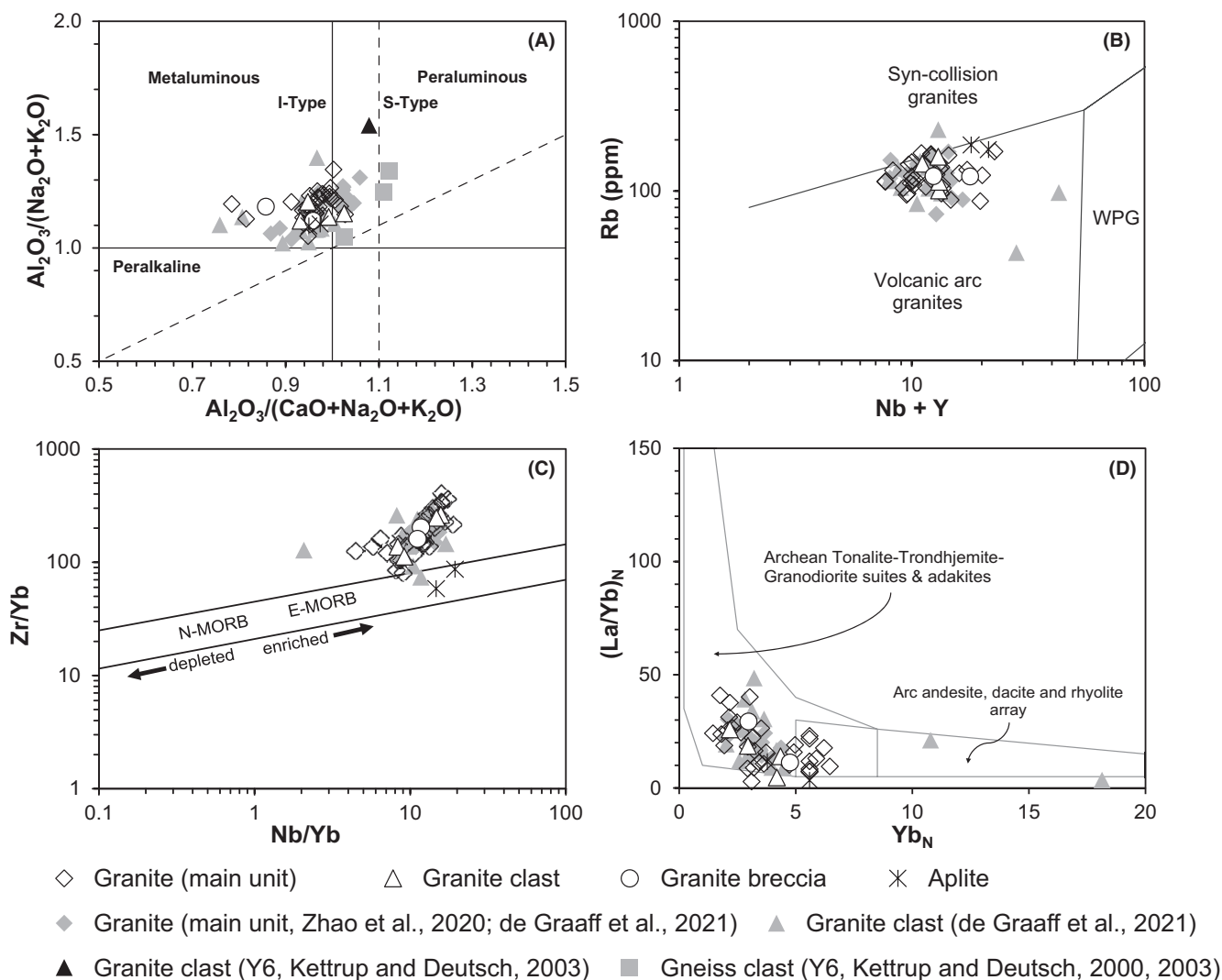


Fig. 10. A) A/NK versus A/CNK discriminating diagram, with A = Al_2O_3 , C = CaO, N = Na_2O , and K = K_2O , all in molar proportions (modified from Maniar and Picolli 1989). The majority of the investigated granites in M0077A core are metaluminous with a weakly peraluminous character, associated with I-Type granites. Y6 clasts have a more peraluminous affinity. None of the investigated samples show a peralkaline character. B) Rb versus Nb + Y diagram, discriminating the granite tectonic context, as defined by Pearce et al. (1984). WPG = within-plate granite. The M0077A core granites are characterized as volcanic arc granite, with only one sample plotting in the syn-collision granite array. C) Zr/Yb versus Nb/Yb diagram (modified from Macdonald et al. 2000). N-MORB = normal mid-oceanic ridge basalt; E-MORB = enriched mid-oceanic ridge basalt. The granite, granite clast, and breccia samples plot outside the MORB array, indicating that they are derived from a different source, probably enriched. However, the two aplite samples are located in the E-MORB area, suggesting that they could have formed from a source with a different chemical composition. D) $(\text{La}/\text{Yb})_N$ versus $(\text{Yb})_N$ with the typical fields for adakites and normal-arc volcanic rocks (Martin et al. 2005). A significant number of the granite samples plots in the overlapping area between adakites and “normal” arc-rocks. Interestingly, two granite clasts recovered by de Graaff et al. (2021) have a distinct composition with high $(\text{Yb})_N$ and low $(\text{La}/\text{Yb})_N$ typical for “normal” arc volcanic rocks.

hydrothermal alteration following the impact cannot solely account for the more radiogenic $^{87}\text{Sr}/^{86}\text{Sr}$ ratios measured in 10 of the investigated samples (Table 3).

The apparent age of 273 ± 21 Ma determined by the whole-rock errorchron (Fig. 11C), younger than the Carboniferous ages reported in Zhao et al. (2020) and Ross et al. (2021), indicates that the Rb–Sr system was

likely disrupted (i.e., open system behavior), within ~ 50 Myr after granite crystallization and, thus, could account for another, older, metasomatic event that affected the Chicxulub granite unit. Following this event, the already altered granite was affected by postimpact hydrothermal overprint. Moreover, this apparent age overlaps within uncertainty with the age

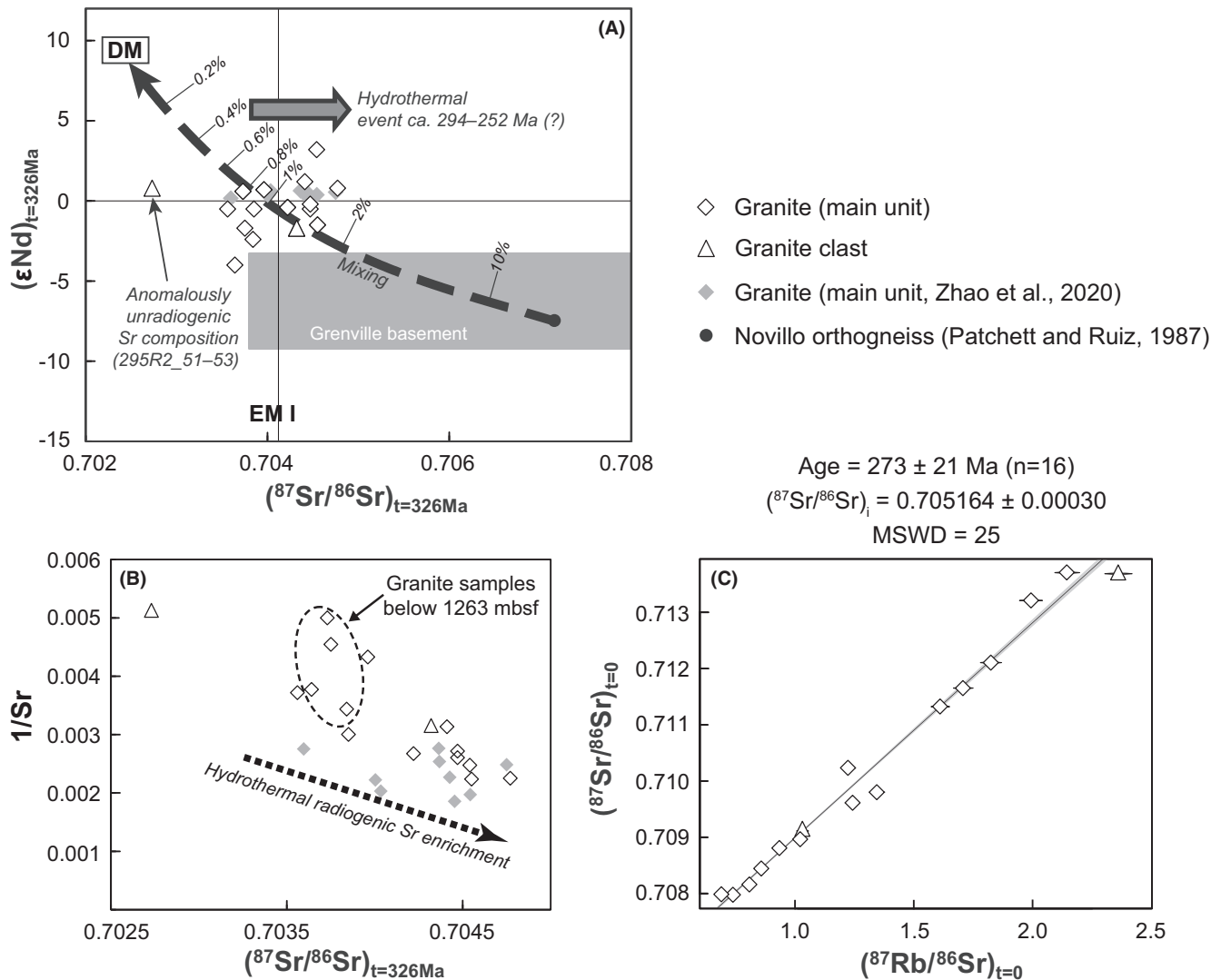


Fig. 11. Strontium–Nd isotopic compositions of 14 granite samples from the main unit and two granite clasts. M0077A granite Sr–Nd isotopic data from Zhao et al. (2020) are also reported for comparison. A) Initial $(\epsilon_{\text{Nd}})_{t=326\text{Ma}}$ and $(^{87}\text{Sr}/^{86}\text{Sr})_{t=326\text{Ma}}$ ratios. The Grenvillian basement area is drawn from data of Patchett and Ruiz (1987) and Weber and Köhler (1999). The Novillo Gneiss composition is from Patchett and Ruiz (1987). The mixing model calculation, DM, and EM I compositions at $t = 326$ Ma are calculated from Faure and Mensing (2004), with DM = depleted mantle, and EM I = enriched mantle I. B) Strontium concentration (expressed as $1/\text{Sr}$) versus initial $(^{87}\text{Sr}/^{86}\text{Sr})_{t=326\text{Ma}}$. With increasing Sr concentration, Sr is becoming more radiogenic and thus may be consistent with addition, a short time after granite crystallization, of radiogenic Sr (and of Rb, to enhance this difference over time) by hydrothermal enrichment. However, the samples in proximity to the LIMB, in the lower part of the granite unit (dashed circle) are among the least Sr-rich (and least radiogenic) and perhaps have experienced more “recent” limited addition of Rb (related with the postimpact hydrothermal system). C) $^{87}\text{Sr}/^{86}\text{Sr}$ versus $^{87}\text{Rb}/^{86}\text{Sr}$. Isochron of all the investigated samples ($n = 16$). A strong scattering is noticed with an MSWD of 25. The uncertainty of age and $(^{87}\text{Sr}/^{86}\text{Sr})_i$ is expressed with a 2σ interval.

recorded in allanite, that is, 215 ± 28 to 260 ± 9 Ma (Wittmann et al. 2018), and, thus, probably corresponds to the same hydrothermal event. Taking into account these parameters, and given the high uncertainty on the apparent age, a metamorphic/hydrothermal fluid metasomatism during the late Triassic, possibly related to the intracontinental extension, which occurred during

the initial breakup of Pangea (Dickinson and Lawton 2001; Steiner 2005), might be the best candidate to explain the apparent Rb–Sr errorchron age and allanite ages.

The age-corrected, initial $(^{87}\text{Sr}/^{86}\text{Sr})_{t=326\text{Ma}}$ and $(\epsilon_{\text{Nd}})_{t=326\text{Ma}}$ compositions suggest that the granites may have formed following a mixing between a mantle-

derived component, which could be relatively similar in composition to the Pan-African Stony Mountain gabbro (Pollock and Hibbard 2010), as suggested by Zhao et al. (2020), and a minor contribution of a moderately enriched, Grenvillian, crustal component, which could be similar to the Novillo Gneiss (Fig. 11A), located in the Oaxaquian crust, in northeastern Mexico (Patchett and Ruiz 1987), even though the data display some scattering. The presence of a Grenvillian component is suggested by the $T_{DM2}(t=326\text{Ma})$ of 0.8–1.4 Ga recorded by the samples. Additionally, the assimilation of the Oaxaquian crust in the Pan-African granitoids of the northern Maya block was previously suggested by Lopez et al. (2001). Three granite samples (156R3_11–15, 229R2_62–67, and 266R2_95.5–98.5) plot in the +ve area (i.e., displaying positive $[\epsilon_{Nd}]_{t=326\text{Ma}}$ and radiogenic $[\text{}^{87}\text{Sr}/\text{}^{86}\text{Sr}]_{t=326\text{Ma}}$, see Fig. 11A). These samples, albeit not showing strong evidence for mineral deformation, are cross-cut by shear fractures (however, it cannot be excluded that these features were formed following the impact) or, in the case of sample 229R2_62–67, are in contact with aplite, which enhanced fluid circulation. They infer addition of radiogenic Sr but not evolved Nd, thus indicating consistent hydrothermal fluid metasomatism. Given the apparent Rb-Sr errorchron and allanite ages, the Late Triassic metasomatic event could explain these three specific compositions, by possibly adding metasomatic Rb in a relatively short timescale after granite crystallization. The possibility of metasomatic ^{87}Rb enrichment is also indicated by the $(\text{}^{87}\text{Sr}/\text{}^{86}\text{Sr})_{t=326\text{Ma}}$ becoming more radiogenic with increasing Sr concentration (Faure and Mensing 2004) (Fig. 11B).

The granite clast sample 295R2_51–53 displays a distinctly lower initial $(\text{}^{87}\text{Sr}/\text{}^{86}\text{Sr})_{t=326\text{Ma}}$ of 0.70273 and not evolved $(\epsilon_{Nd})_{t=326\text{Ma}}$ of 0.8, while having the highest $^{87}\text{Rb}/\text{}^{86}\text{Sr}$ (2.3614) of all investigated samples. Petrologically, this sample is highly deformed, with mineral ductile deformation and pervasive shear fracture networks throughout, which could be either a record of the late Triassic metamorphic event, or of postimpact deformation. Addition of Rb during the onset of the postimpact hydrothermal system, at temperatures of ~300–400 °C as estimated by Kring et al. (2020) and Simpson et al. (2020), may explain the particular composition of this sample, as this “recent” Rb would not have had the time to decay. Interestingly, granite samples from the lower part of the granite unit (below 1263 mbsf, $n = 4$) may also have been affected, to a lesser extent, by this “recent” Rb enrichment related to the postimpact hydrothermal system (Fig. 11B), as they display more radiogenic $^{87}\text{Sr}/\text{}^{86}\text{Sr}$ (average 0.712196) and higher $^{87}\text{Rb}/\text{}^{86}\text{Sr}$ (average 1.82265) compared to the granite samples in the upper

part of the granite unit (average $^{87}\text{Sr}/\text{}^{86}\text{Sr}$ and $^{87}\text{Rb}/\text{}^{86}\text{Sr}$ of 0.709319 and 1.08574, respectively), and thus back-calculate to unradiogenic $(\text{}^{87}\text{Sr}/\text{}^{86}\text{Sr})_{t=326\text{Ma}}$ with an average of 0.703740. However, the Sr depletion observed in these granites and possibly related to hydrothermal alteration of plagioclase (sericitization), could also explain these compositions and may have occurred either (or both) during the Late Triassic metasomatic event or during the postimpact alteration, although the latter is more probable as the Sr depletion only occurs in the lower granite samples, in proximity to the LIMB and cataclastites.

The available data seem to indicate that the Chicxulub peak ring granites were affected by at least two hydrothermal alteration/metasomatic events, that is, a first event taking place approximately 50 Myr after granite formation (273 ± 21 Ma), and a second event related to the postimpact hydrothermal alteration (as the result of a hydrothermal system active for more than 1 Myr after the impact event at 66.05 Ma). However, some care should be taken in these interpretations, as it is not possible to fully disentangle the specific effects of the Late Triassic metasomatic event from the postimpact hydrothermal alteration event. In addition, the granite samples may not have kept their original magmatic Rb-Sr isotopic signature due to these alteration events.

Comparison with Granitoid Lithologies from the Chicxulub Impact Structure

Geochemical data available for granitoid rocks (clasts) from other drill cores recovered inside the Chicxulub impact structure were compared to the obtained results (Figs. 7–11). The geochemistry of nine granite samples from the “lower peak-ring” section of the Hole M0077A drill core was investigated by Zhao et al. (2020), while six granites from the main unit and 18 granite clasts were investigated by de Graaff et al. (2021). Major and trace element compositions of the granite samples from the main unit and the majority of the clasts in Zhao et al. (2020) and de Graaff et al. (2021) show no significant differences from the samples in this study, albeit a minor Eu negative anomaly with an Eu^* of 0.77 ± 0.02 ($\text{Eu}^* = \text{Eu}_N/[\text{Sm}_N \times \text{Gd}_N]^{0.5}$) was recorded in four granite clasts and one granite from the main unit in de Graaff et al. (2021). Moreover, de Graaff et al. (2021) describe a granitic clast with a syenite composition (13.3 wt% $\text{Na}_2\text{O} + \text{K}_2\text{O}$), and two granitic samples at 730.3 and 1287.8 mbsf with distinct enrichments in the HREE and LREE contents (Fig. 8). Additionally, these two granite clasts show a distinct Sr/Y, $(\text{La}/\text{Yb})_N$, Y, and $(\text{Yb})_N$ (Fig. 10D), which is most comparable to “normal” arc-related rocks. The former

was interpreted to be a textural characteristic related to it being an alkali-feldspar dominated sample while the latter two clasts were interpreted to either reflect granite clasts that were significantly affected by an interaction with the host impact melt rock or they were derived from a granitic body distinct from the main granite unit sampled in the Hole M0077A core (de Graaff et al. 2021).

Based on the investigation of a limited number of granite samples, Zhao et al. (2020) characterized the granites as “adakitic rocks” due to their anomalously high Sr/Y and $(La/Yb)_N$ ratios and low Y content and low $(Yb)_N$. However, the term “adakite” (or “adakitic”) is often used to cover a large range of rocks with different characteristics and/or formation processes (Moyen 2009). More conservatively applied, the term adakite is restricted to the type of rock called “high silica adakite” (HSA), which is formed by the melting of metabasalts from oceanic crust slab (e.g., Martin et al. 2005). High Sr/Y and $(La/Yb)_N$ ratios are not the only criteria used to define an adakite; thus, in order to decipher the “adakitic” nature of the Chicxulub granites, the parameters defined by Defant and Drummond (1990), Martin et al. (2005), and Moyen (2009) were used in this work. A comparative table summarizes the difference between HSA rocks and the investigated granites (Table 4).

In this study, the investigated granites yield Sr/Y and $(La/Yb)_N$ ratios with wide variations, from 22 to 123 and 3 to 41, respectively. Based on $(La/Yb)_N$ versus $(Yb)_N$, the granites effectively plot in the adakite field as defined in Martin et al. (2005) (Fig. 10D). However, an overlap between adakitic compositions and “normal” arc compositions is noticeable in this diagram, and in

addition, de Graaff et al. (2021) demonstrated that La was mobilized by alteration processes. It is important to highlight here that the investigated aplite samples yield values of Sr/Y and $(La/Yb)_N$ of 26 and 7.5, below the adakitic thresholds of 40 and 10, respectively (Table 4). In addition, with Al_2O_3 content below 15 wt%, FeO + MgO + MnO + TiO_2 contents <7 wt%, Mg# <50, K_2O/Na_2O above 0.4 (revealing a more potassic composition), and low Cr and Ni contents (suggesting a more evolved source), the investigated granites are distinctly different from a typical “adakitic rock.” In addition, in the Zr/Yb versus Nb/Yb diagram (Fig. 10C), the granites, granite clasts, and granite breccias plot outside the MORB array, further supporting a contribution of an enriched (or possibly crustal) endmember in the granite genesis. Combined with the Nd isotopic data, this indicates a formation process distinct from adakites (Moyen 2009). Thus, the investigated granites should be termed high-K (high-Sr/Y or high $(La/Yb)_N$), calc-alkaline granites.

Granite-like lithologies were also sampled and investigated in the Y6 core (Kettrup et al. 2000; Kettrup and Deutsch 2003), that is, one granite and four granitic gneiss clasts in the suevite. Only major element and Sr–Nd isotopic data are available for these clast samples. The Y6 granite clast shows a composition distinct from the Expedition 364 granite samples and is highly silicic (81.9 wt% SiO_2) and subalkaline. The gneiss clast samples exhibit more variations with 67.9–84.3 wt% SiO_2 and have peraluminous compositions. These distinct compositions highlight the variety of evolved lithologies represented in the Yucatán peninsula crystalline basement and found as clasts in impact breccia and impact melt rock samples.

Table 4. Comparison between the average composition of the high silica adakite (HSA) and the investigated granites samples from the Expedition 364 Chicxulub drill core, using all the criteria defined for adakitic rocks in addition to Sr/Y and $(La/Yb)_N$ ratios (Defant and Drummond 1990; Martin et al. 2005; Moyen 2009).

	HSA Adakites average values*	Average granites	Average granite clasts	Average granite breccias	Average aprites
SiO_2 (wt%)	>56	73.1	74.4	71.1	74.7
Al_2O_3 (wt%)	>15	14	13	14	14
MgO (wt%)	<3	0.6	0.5	0.9	0.1
FeO + MgO + MnO + TiO_2 (wt %)	≈7	2.0	1.8	2.6	0.7
Mg#	≈50	38	41	44	22
K_2O/Na_2O	≈0.4	0.8	0.9	0.8	0.9
Y (ppm)	<18	6.0	6.5	8.1	7.2
Yb (ppm)	<1.9	0.6	0.6	0.6	0.8
Cr (ppm)	≈36	19	11	26	13
Ni (ppm)	≈24	3.9	4.5	9.4	0.7
Sr/Y	>40	62	50	40	26
$(La/Yb)_N$	>10	19	16	20	7.5

*As defined by Defant and Drummond (1990), Martin et al. (2005), and Moyen (2009).

While the Sr–Nd isotopic composition recorded by Zhao et al. (2020) is similar to our “group 1” (i.e., the least altered granites), the Sr–Nd isotopic ratios of the Y6 granite and three of the gneiss clasts exhibit distinct, more enriched crustal signatures (Fig. 11). The fourth gneiss clast (Y6 N14 p4a) has a high $(^{87}\text{Sr}/^{86}\text{Sr})_{t=0}$ of 0.732676 and chondritic $(\epsilon_{\text{Nd}})_{t=0}$ of 0.0, and represents another, distinct component of the Yucatán target (Kettrup and Deutsch 2003).

The Nd model ages (one- or two-stage model ages termed as T_{DM1} and T_{DM2} , respectively) calculated for the most primitive samples ($T_{\text{DM2}(326\text{Ma})}$ of 0.8–1.2 Ga) encompass the calculated model age range of Zhao et al. (2020), with $T_{\text{DM2}(326\text{Ma})}$ for the granites between 1.0 and 1.1 Ga. Crystalline basement clasts recovered within impact breccia and impact melt rocks yield T_{DM1} between 0.7 and 1.4 Ga, while impact melt rocks have T_{DM1} of 1.1–1.2 Ga (Kettrup et al. 2000; Kettrup and Deutsch 2003; Keppie et al. 2011). This implies that the northern Maya block and the granite investigated here involved Grenville-aged material during their formation (Keppie et al. 2012).

In general, our results are consistent with previous studies on a more limited set of samples (see Zhao et al. 2020; de Graaff et al. 2021), and further support that the investigated granite unit could be related with arc magmatism during the closure of the Rheic ocean and Pangea assembly in the Carboniferous (Zhao et al. 2020; Ross et al. 2021). Conversely, a similar granite type was not sampled in any previous drill cores, including Y6 (Kettrup et al. 2000; Kettrup and Deutsch 2003). However, the Expedition 364 drill core offers only a limited view of the extension of this granite unit; thus, care should be taken when discussing geodynamic implications of the data.

CONCLUSIONS

The granite from the “lower peak-ring” section in the IODP-ICDP Expedition 364 Hole M0077A drill core can be defined as coarse-grained, phaneritic with K-feldspar (orthoclase), plagioclase, quartz, and biotite as the main mineral phases. In addition to the main granite unit, granite clasts, granite breccias, and aplites and pegmatites are observed. Impact-induced deformations are pervasive with fracturing, shearing, and the presence of cataclasite veins and shock metamorphic features in minerals (such as PFs, FFs, and PDFs in quartz, but also a large set of shock metamorphic features in all other minerals composing the granites).

Despite numerous textural changes, the chemical composition of the granite inside the peak ring is broadly homogeneous and defines the studied samples

as high-K (high-Sr/Y or high $[\text{La}/\text{Yb}]_N$), calc-alkaline granites.

The major and trace element patterns suggest a formation by fractional crystallization with moderate plagioclase fractionation. However, initial Sr–Nd isotopic data reveal a more complex origin, with admixture of a Grenvillian crust component during the granite genesis, as suggested by the two-stage Nd model ages $T_{\text{DM2}(326\text{Ma})}$ of 0.8–1.2 Ga. Additionally, the granite experienced a hydrothermal fluid metasomatic/metamorphic event, indicated by the radiogenic Sr enrichment and allanite crystallization. An apparent errorchron age of 273 ± 21 Ma indicates that this may be related to the intracontinental extension that occurred at the Yucatán peninsula during the late Triassic initial breakup of Pangea. However, the high uncertainty on the apparent age may also reflect the effect of postimpact alteration, which is also recorded in the granites, and thus disturbed the Rb–Sr system even more, adding complexity to the data interpretation. Additionally, the granites in the vicinity of impact melt rock or cataclasite dikes, mainly in the lower part of the granite unit, seem to have experienced, to some extent, alteration from the long-lasting, postimpact hydrothermal system, through addition of more recent Rb. Strontium depletion, related to the hydrothermal alteration of plagioclase, is also observed in these samples, without allowing any conclusion on which hydrothermal event was the cause of this Sr depletion. Other fluid mobile elements, such as Ba, Th, and U, have also been affected, probably by both hydrothermal events.

Our results are consistent with previous work conducted on granite samples recovered at site M0077, supporting that the calc-alkaline to high-K calc-alkaline granites located in the Chicxulub impact structure peak ring were formed in an arc tectonic context, intruding the Maya block during the closure of the Rheic ocean and assembly of Pangea.

Acknowledgments—This paper is dedicated to the memory of Hervé Martin (1951–2021) who developed the well-known “adakitic” model, constituting a reference in the characterization of adakites and related rocks. The Chicxulub drilling was funded by the IODP as Expedition 364, with co-funding from ICDP. Expedition 364 was implemented by ECORD, with contributions and logistical support from the Yucatán state government and Universidad Nacional Autónoma de México. Partial funding was provided by the University of Vienna doctoral school IK-1045 (P.I.: C.K.). We thank Peter Nagl and Marianne Schwarzingler for XRF sample preparation and analysis, Dieter Mader for INAA and data processing, and

Monika Horschinegg and Wencke Wegner for sample preparation and TIMS Sr–Nd isotopic analysis. J.-G. F. thanks Wencke Wegner for constructive discussions on Sr–Nd isotopic data interpretation, and Jiawei Zhao for general discussions. The AMGC team is supported by Research Foundation Flanders (FWO-Vlaanderen) and BELSPO; P.K. is an FWO PhD fellow (project 11E6619N; 11E6621N). S.G. and P.C. thank the EoS project “ET-HoME” for support and the VUB Strategic Research Program. P.C. thanks the FWO—Hercules Program for financing the μ XRF instrument at the VUB. J.-G. F. thanks Jean-François Moyen for valuable comments on adakites and granites in general. We thank Lutz Hecht and Stephen Prevec for their detailed and constructive reviews, as well as Jeffrey Plescia for editorial handling.

The authors declare no conflict of interest.

Data Availability Statement—The data that support the findings of this study are available in the supplementary material of this article.

Editorial Handling—Dr. Jeffrey Plescia

REFERENCES

- Alaniz-Álvarez S. A., van der Heyden P., Nieto-Samaniego A. F., and Ortega-Gutiérrez F. 1996. Radiometric and kinematic evidence for Middle Jurassic strike-slip faulting in southern Mexico related to the opening of the Gulf of Mexico. *Geology* 24:443–446.
- Belza J., Goderis S., Keppens E., Vanhaecke F., and Claeys P. 2012. An emplacement mechanism for the mega-block zone within the Chicxulub crater (Yucatán, Mexico) based on chemostratigraphy. *Meteoritics & Planetary Science* 47:400–413.
- Belza J., Goderis S., Smit J., Vanhaecke F., Baert K., Terryn H., and Claeys P. 2015. High spatial resolution geochemistry and textural characteristics of ‘microtektite’ glass spherules in proximal Cretaceous–Paleogene sections: Insights into glass alteration patterns and precursor melt lithologies. *Geochimica et Cosmochimica Acta* 152:1–38.
- Brooks C., Hart S. R., and Wendt I. 1972. Realistic use of two-error regression treatment as applied to rubidium–strontium data. *Reviews of Geophysics and Space Physics* 10:551–557.
- Chiarenza A. A., Farnsworth A., Mannion P. D., Lunt D. J., Valdes P. J., Morgan J. V., and Allison P. A. 2020. Asteroid impact, not volcanism, caused the end-Cretaceous dinosaur extinction. *Proceedings of the National Academy of Sciences* 117:17,084–17,093.
- Claeys P., Heuschkel S., Lounejeva-Baturina E., Sanchez-Rubio G., and Stöffler D. 2003. The suevite of drill hole Yucatán 6 in the Chicxulub impact crater. *Meteoritics & Planetary Science* 38:1299–1317.
- Collins G. S., Patel N., Davison T. M., Rae A. S. P., Morgan J. V., Gulick S. P. S., IODP-ICDP Expedition 364 Science Party, and Third-Party Scientists. 2020. A steeply-inclined trajectory for the Chicxulub impact. *Nature Communications* 11:1480. <https://doi.org/10.1038/s41467-020-15269-x>
- Cox M. A., Erickson T. M., Schmieder M., Christoffersen R., Ross D. K., Cavosie A. J., Bland P. A., Kring D. A., and IODP-ICDP Expedition 364 Scientists. 2020. High-resolution microstructural and compositional analyses of shock deformed apatite from the peak ring of the Chicxulub impact crater. *Meteoritics & Planetary Science* 55:1715–1733.
- Cruciani G., Franceschelli M., and Puxeddu M. 2017. U-, Pb-enrichment, Sr-depletion produced by water-rock interaction processes within the eclogitic oceanic crust of Ordovician age in NE Sardinia. *Procedia Earth and Planetary Science* 17:508–511.
- Defant M. J. and Drummond M. S. 1990. Derivation of some modern arc magmas by melting of young subducted lithosphere. *Nature* 347:662–665.
- de Graaff S. J., Kaskes P., Déhais T., Goderis S., Debaille V., Matielli N., Ross C. H., Gulick S. P. S., Feignon J.-G., Ferrière L., Koeberl C., Smit J., and Claeys P. 2021. New insights into the formation and emplacement of impact melt rocks of the Chicxulub impact structure, Mexico, following the 2016 IODP-ICDP Expedition 364. *Geological Society of America Bulletin*. <https://doi.org/10.1130/B35795.1>.
- Dengo G. 1969. Problems of tectonic relations between Central America and the Caribbean. *Gulf Coast Association of Geological Societies Transactions* 19:311–320.
- DePaolo D. J. 1981. Trace element and isotopic effects of combined wallrock assimilation and fractional crystallization. *Earth and Planetary Science Letters* 53:189–202.
- DePaolo D. J. and Wasserburg G. J. 1976. Nd isotopic variations and petrogenetic models. *Geochemistry* 3:249–252.
- de Winter N. J. and Claeys P. 2016. Micro X-ray fluorescence (μ XRF) line scanning on Cretaceous rudist bivalves: A new method for reproducible trace element profiles in bivalve calcite. *Sedimentology* 64:231–251.
- Dickinson W. R. and Lawton T. F. 2001. Carboniferous to Cretaceous assembly and fragmentation of Mexico. *Geological Society of America Bulletin* 113:1142–1160.
- Donnelly T. W., Horne G. S., Finch R. C., and López-Ramos E. 1990. Northern Central America; the Maya and Chortis blocks. In *The Caribbean region; The Geology of North America*, edited by Dengo G. and Case J. E. Boulder, Colorado: Geological Society of America. pp. 371–396.
- Dressler B. O., Sharpton V. L., Morgan J., Moran D., Smit J., Stöffler D., and Urrutia J. 2003. Investigating a 65-Ma-old smoking gun: Deep drilling of the Chicxulub impact structure. *Eos, Transactions, American Geophysical Union* 84:125–130.
- Ewart A. 1982. The mineralogy and petrology of Tertiary-recent orogenic volcanic rocks: With a special reference to the andesitic-basaltic compositional range. In *Andesites: Orogenic andesites and related rocks*, edited by Thorpe R. S. Chichester, UK: Wiley. pp. 25–95.
- Faure G. and Mensing T. M. 2004. *Isotopes: Principles and applications*. Hoboken, New Jersey: John Wiley & Sons Inc.
- Feignon J.-G., Ferrière L., Leroux H., and Koeberl C. 2020. Characterization of shocked quartz grains from Chicxulub peak ring granites and shock pressure estimates. *Meteoritics & Planetary Science* 55:2206–2223.

- Ferrière L., Rae A. S. P., Poelchau M., Koeberl C., and the IODP-ICDP Expedition 364 Science Party. 2017. Macro- and microscopic evidence of impact metamorphism in rocks from the Chicxulub peak ring IODP-ICDP expedition 364 drill core (abstract #1600). 48th Lunar and Planetary Science Conference. CD-ROM.
- Goderis S., Sato H., Ferrière L., Schmitz B., Burney D., Kaskes P., Vellekoop J., Wittmann A., Schulz T., Chernozhukhin S. M., Claeys P., de Graaff S. J., Déhais T., de Winter N. J., Elfman M., Feignon J.-G., Ishikawa A., Koeberl C., Kristiansson P., Neal C. R., Owens J. D., Schmieder M., Sinnesael M., Vanhaecke F., Van Malderen S. J. M., Bralower T. J., Gulick S. P. S., Kring D. A., Lowery C. M., Morgan J. V., Smit J., Whalen M. T., and IODP-ICDP Expedition 364 Scientists. 2021. Globally distributed iridium layer preserved within the Chicxulub impact structure. *Science Advances* 7:abe3647.
- Goderis S., Tagle R., Belza J., Smit J., Montanari A., Vanhaecke F., Erzinger J., and Claeys P. 2013. Reevaluation of siderophile element abundances and ratios across the Cretaceous-Paleogene (K-Pg) boundary: Implications for the nature of the projectile. *Geochimica et Cosmochimica Acta* 120:417–446.
- Gulick S. P. S., Barton P. J., Christeson G. L., Morgan J. V., McDonald M., Mendoza-Cervantes K., Pearson Z. F., Surendra A., Urrutia-Fucugauchi J., Vermeesch P. M., and Warner M. R. 2008. Importance of pre-impact crustal structure for the asymmetry of the Chicxulub impact crater. *Nature Geoscience* 1:131–135.
- Gulick S. P. S., Christeson G. L., Barton P. J., Grieve R. A. F., Morgan J. V., and Urrutia-Fucugauchi J. 2013. Geophysical characterization of the Chicxulub impact crater. *Reviews of Geophysics* 51:31–52.
- Gulick S. P. S., Bralower T. J., Ormö J., Hall B., Grice K., Schaefer B., Lyons S., Freeman K. H., Morgan J. V., Artemieva N., Kaskes P., de Graaff S. J., Whalen M. T., Collins G. S., Tikoo S. M., Verhagen C., Christeson G. L., Claeys P., Coolen M. J. L., Goderis S., Goto K., Grieve R. A. F., McCall N., Osinski G. R., Rae A. S. P., Riller U., Smit J., Vajda V., Wittmann A., and Expedition 364 Scientists. 2019. The first day of the Cenozoic. *Proceedings of the National Academy of Sciences* 116:19,342–19,351.
- Hecht L., Wittmann A., Schmitt R.-T., and Stöffler D. 2004. Composition of impact melt particles and the effects of post-impact alteration in suevitic rocks at the Yaxcopoil-1 drill core, Chicxulub crater, Mexico. *Meteoritics & Planetary Science* 39:1169–1186.
- Helvacı C. and Griffin W. L. 1983. Metamorphic feldspathization of metavolcanics and granitoids, Avnik area, Turkey. *Contributions to Mineralogy and Petrology* 83:309–319.
- Hildebrand A. R., Penfield G. T., Kring D. A., Pilkington M., Camargo Z. A., Jacobsen S. B., and Boynton W. V. 1991. Chicxulub crater: A possible Cretaceous/Tertiary boundary impact crater on the Yucatán Peninsula, Mexico. *Geology* 19:867–871.
- Hsu W. 2003. Rare earth element geochemistry and petrogenesis of Miles (IIE) silicate inclusions. *Geochimica et Cosmochimica Acta* 67:4807–4821.
- Kamo S. L. and Krogh T. E. 1995. Chicxulub crater source for shocked zircon crystals from the Cretaceous-Tertiary boundary layer, Saskatchewan: Evidence from new U-Pb data. *Geology* 23:281–284.
- Kamo S. L., Lana C., and Morgan J. V. 2011. U-Pb ages of shocked zircon grains link distal K-Pg boundary sites in Spain and Italy with the Chicxulub impact. *Earth and Planetary Science Letters* 310:401–408.
- Kaskes P., Déhais T., de Graaff S. J., Goderis S., and Claeys P. 2021. Micro-X-ray fluorescence (μ XRF) analysis of proximal impactites: High-resolution element mapping, digital image analysis, and quantifications. In *Large meteorite impacts and planetary evolution VI: Geological Society of America special paper 550*, edited by Reimold W. U. and Koeberl C. Boulder, Colorado: Geological Society of America. pp. 171–206. [https://doi.org/10.1130/2021.2550\(07\)](https://doi.org/10.1130/2021.2550(07))
- Keppie J. D., Dostal J., Norman M., Urrutia-Fucugauchi J., and Grajales-Nishimura M. 2011. Study of melt and a clast of 546 Ma magmatic arc rocks in the 65 Ma Chicxulub bolide breccia, northern Maya block, Mexico: Western limit of Ediacaran arc peripheral to northern Gondwana. *International Geology Review* 53:1180–1193.
- Keppie J. D., Murphy J. B., Nance R. D., and Dostal J. 2012. Mesoproterozoic Oaxaquia-type basement in peri-Gondwanan terranes of Mexico, the Appalachians and Europe: T_{DM} age constraints on extent and significance. *International Geology Review* 54:313–324.
- Kettrup B. and Deutsch A. 2003. Geochemical variability of the Yucatán basement: Constraints from crystalline clasts in Chicxulub impactites. *Meteoritics & Planetary Science* 38:1079–1092.
- Kettrup B., Deutsch A., Ostermann M., and Agrinier P. 2000. Chicxulub impactites: Geochemical clues to the precursor rocks. *Meteoritics & Planetary Science* 35:1229–1238.
- Koeberl C. 1993a. Chicxulub crater, Yucatán: Tektites, impact glasses, and the geochemistry of target rocks and breccias. *Geology* 21:211–214.
- Koeberl C. 1993b. Instrumental neutron activation analysis of geochemical and cosmochemical samples: A fast and reliable method for small sample analysis. *Journal of Radioanalytical and Nuclear Chemistry* 168:47–60.
- Koeberl C. and Sigurdsson H. 1992. Geochemistry of impact glasses from the K/T boundary in Haiti: Relation to smectites and a new type of glass. *Geochimica et Cosmochimica Acta* 56:2113–2129.
- Kring D. A. 2005. Hypervelocity collisions into continental crust composed of sediments and an underlying crystalline basement: Comparing the Ries (~24 km) and Chicxulub (~180 km) impact craters. *Geochemistry* 65:1–46.
- Kring D. A. and Boynton W. V. 1992. Petrogenesis of an augite-bearing melt rock in the Chicxulub structure and its relationship to K/T impact spherules in Haiti. *Nature* 358:141–144.
- Kring D. A., Tikoo S. M., Schmieder M., Riller U., Rebolledo-Vieyra M., Simpson S. L., Osinski G. R., Gattacceca J., Wittmann A., Verhagen C. M., Cockell C. S., Coolen M. J. L., Longstaffe F. J., Gulick S. P. S., Morgan J. V., Bralower T. J., Chenot E., Christeson G. L., Claeys P., Ferrière L., Gebhardt C., Goto K., Green S. L., Jones H., Lofi J., Lowery C. M., Ocampo-Torres R., Perez-Cruz L., Pickersgill A. E., Poelchau M. H., Rae A. S. P., Rasmussen C., Sato H., Smit J., Tomioka N., Urrutia-Fucugauchi J., Whalen M. T., Xiao L., and Yamaguchi K. E. 2020. Probing the hydrothermal system of the Chicxulub impact crater. *Science Advances* 6:eaaz3053.
- Krogh T. E., Kamo S. L., Sharpton V. L., Marin L. E., and Hildebrand A. R. 1993. U-Pb ages of single shocked

- zircons linking distal K/T ejecta to the Chicxulub crater. *Nature* 366:731–734.
- Langmuir C. H., Klein E. M., and Plank T. 1992. Petrological systematics of mid-ocean ridge basalts: Constraints on melt generation beneath oceanic ridges. In *Mantle flow and melt generation at mid-ocean ridges*, edited by Morgan J. P., Blackman D. K., and Sinton J. M. Geophysical Monograph Series, Volume 71. Washington, D.C.: American Geophysical Union. pp. 183–280.
- Liew T. C. and Hofmann A. W. 1988. Precambrian crustal components, plutonic associations, plate environment of the Hercynian fold belt of central Europe: Indications from a Nd and Sr isotopic study. *Contributions to Mineralogy and Petrology* 98:129–138.
- Lopez R., Cameron K. L., and Jones N. W. 2001. Evidence for Paleoproterozoic, Grenvillian and Pan-African age Gondwana crust beneath northeastern Mexico. *Precambrian Research* 107:195–214.
- Lopez Ramos E. 1975. Geological summary of the Yucatan peninsula. In *The Gulf of Mexico and the Caribbean*, edited by Nairn A. E. M. and Stehli F. G. Boston, Massachusetts: Springer. pp. 257–282.
- Macdonald R., Hawkesworth C. J., and Heath E. 2000. The Lesser Antilles volcanic chain: A study in arc magmatism. *Earth-Science Reviews* 49:1–76.
- Mader D. and Koeberl C. 2009. Using instrumental neutron activation analysis for geochemical analyses of terrestrial impact structures: Current analytical procedures at the University of Vienna Geochemistry Activation Analysis Laboratory. *Applied Radiation and Isotopes* 67:2100–2103.
- Maniar P. D. and Piccoli P. M. 1989. Tectonic discrimination of granitoids. *Geological Society of America Bulletin* 101:635–643.
- Martin H., Smithies R. H., Rapp R. P., Moyon J.-F., and Champion D. C. 2005. An overview of adakite, tonalite-trondjhemite-granodiorite (TTG) and sanukitoid: Relationships and some implications for crustal evolution. *Lithos* 79:1–24.
- McDonough W. F. and Sun S. 1995. The composition of the Earth. *Chemical Geology* 120:223–253.
- Middlemost E. A. K. 1994. Naming materials in the magma/igneous rock system. *Earth-Science Reviews* 37:215–224.
- Morgan J., Warner M., the Chicxulub Working Group, Brittan J., Buffler R., Camargo A., Christeson G., Denton P., Hildebrand A., Hobbs R., Macintyre H., Mackenzie G., Maguire P., Marin L., Nakamura Y., Pilkington M., Sharpton V., Snyder D., Suarez G., and Trejo A. 1997. Size and morphology of the Chicxulub impact crater. *Nature* 390:472–476.
- Morgan J. V., Gulick S. P. S., Bralower T., Chenot E., Christeson G., Claeys P., Cockell C., Collins G. S., Coolen M. J. L., Ferrière L., Gebhardt C., Goto K., Jones H., Kring D. A., Le Ber E., Lofi J., Long X., Lowery C., Mellett C., Ocampo-Torres R., Osinski G. R., Perez-Cruz L., Pickersgill A., Pöschel M., Rae A., Rasmussen C., Rebolledo-Vieyra M., Riller U., Sato H., Schmitt D. R., Smit J., Tikoo S., Tomioka N., Urrutia-Fucugauchi J., Whalen M., Wittmann A., Yamaguchi K. E., and Zylberman W. 2016. The formation of peak rings in large impact craters. *Science* 354:878–882.
- Morgan J., Gulick S., Mellett C. L., Green S. L., and Expedition 364 Scientists. 2017. *Chicxulub: Drilling the K-Pg impact crater*. Proceedings of the International Ocean Discovery Program, 364. College Station, Texas: International Ocean Discovery Program. 164 p.
- Moyon J.-F. 2009. High Sr/Y and La/Yb ratios: The meaning of the “adakitic signature.” *Lithos* 112:556–574.
- Nagl P. and Mader D. 2019. X-ray fluorescence (XRF) and instrumental neutron activation analysis (INAA) for the geochemical analysis of rocks, presented on in-house control samples (abstract). *Mitteilungen der Österreichischen Mineralogischen Gesellschaft* 165:67.
- Nisbet E. G., Dietrich V. J., and Esenwien A. 1979. Routine trace element determinations in silicate minerals and rocks by X-ray fluorescence. *Fortschritte der Mineralogie* 57:264–279.
- Ortega-Gutiérrez F., Elías-Herrera M., Morán-Zenteno D. J., Solari L., Weber B., and Luna-González L. 2018. The pre-Mesozoic metamorphic basement of Mexico, 1.5 billion years of crustal evolution. *Earth-Science Reviews* 183:2–37.
- Patchett P. J. and Ruiz J. 1987. Nd isotopic ages of crust formation and metamorphism in the Precambrian of eastern and southern Mexico. *Contributions to Mineralogy and Petrology* 96:523–528.
- Pearce J. A. 2014. Immobile element fingerprinting of ophiolites. *Elements* 10:101–108.
- Pearce J. A., Harris N. B. W., and Tindle A. G. 1984. Trace element discrimination diagrams for the tectonic interpretation of granitic rocks. *Journal of Petrology* 25:956–983.
- Penfield G. T. and Camargo Z. A. 1981. Definition of a major igneous zone in the central Yucatán platform with aeromagnetics and gravity. *Society of Exploration Geophysicists Technical Program, Abstracts, and Biographies* 51:37.
- Pittarello L., Ferrière L., Feignon J.-G., Osinski G. R., and Koeberl C. 2020. Preferred orientation distribution of shock-induced planar microstructures in quartz and feldspar. *Meteoritics & Planetary Science* 55:1082–1092.
- Plimer I. R. and Elliott S. M. 1979. The use of Rb/Sr ratios as guide to mineralization. *Journal of Geochemical Exploration* 12:21–34.
- Pollock J. C. and Hibbard J. P. 2010. Geochemistry and tectonic significance of the Stony Mountain gabbro, North Carolina: Implications for the Early Paleozoic evolution of Carolina. *Gondwana Research* 17:500–515.
- Quitté G., Robin E., Levasseur S., Capmas F., Rocchia R., Birc J.-L., and Allègre C. J. 2007. Osmium, tungsten, and chromium isotopes in sediments and in Ni-rich spinel at the K-T boundary: Signature of a chondritic impactor. *Meteoritics & Planetary Science* 42:1567–1580.
- Rae A. S. P., Collins G. S., Poelchau M., Riller U., Davison T. M., Grieve R. A. F., Osinski G. R., Morgan J. V., and IODP-ICDP Expedition 364 Scientists. 2019. Stress-strain evolution during peak-ring formation: A case study of the Chicxulub impact structure. *Journal of Geophysical Research: Planets* 124:396–417.
- Rasmussen C., Stockli D. F., Ross C. H., Pickersgill A., Gulick S. P., Schmieder M., Christeson G. L., Wittmann A., Kring D. A., Morgan J. V., and Expedition 364 Science Party. 2019. U-Pb memory behavior in Chicxulub’s peak ring—Applying U-Pb depth profiling to shocked zircon. *Chemical Geology* 525:356–367.
- Riller U., Poelchau M. H., Rae A. S. P., Schulte F. M., Collins G. S., Melosh H. J., Grieve R. A. F., Morgan J. V., Gulick S. P. S., Lofi J., Diaw A., McCall N., Kring D.

- A., and IODP-ICDP Expedition 364 Science Party. 2018. Rock fluidization during peak-ring formation of large impact structures. *Nature* 562:511–518.
- Ross C. H., Stockli D. F., Rasmussen C., Gulick S. P. S., de Graaff S. J., Claeys P., Zhao J., Xiao L., Pickersgill A. E., Schmieder M., Kring D. A., Wittmann A., and Morgan J. 2021. Evidence of Carboniferous arc magmatism preserved in the Chicxulub impact structure. *Geological Society of America Bulletin*. <https://doi.org/10.1130/B35831.1>.
- Schmieder M., Shaulis B. J., Lapen T. J., and Kring D. A. 2017. U–Th–Pb systematics in zircon and apatite from the Chicxulub impact crater, Yucatán, Mexico. *Geological Magazine* 155:1330–1350.
- Schmitt R. T., Wittmann A., and Stöffler D. 2004. Geochemistry of drill core samples from Yaxcopoil-1, Chicxulub impact crater, Mexico. *Meteoritics & Planetary Science* 39:979–1001.
- Schulte P., Alegret L., Arenillas I., Arz J. A., Barton P. J., Bown P. R., Bralower T. J., Christeson G. L., Claeys P., Cockell C. S., Collins G. S., Deutsch A., Goldin T. J., Goto K., Grajales-Nishimura J. M., Grieve R. A. F., Gulick S. P. S., Johnson K. R., Kiessling W., Koeberl C., Kring D. A., MacLeod K. G., Matsui T., Melosh J., Montanari A., Morgan J. V., Neal C. R., Nichols D. J., Norris R. D., Pierazzo E., Ravizza G., Rebolledo-Vieyra M., Reimold W. U., Robin E., Salge T., Speijer R. P., Sweet A. R., Urrutia-Fucugauchi J., Vajda V., Whalen M. T., and Willumsen P. S. 2010. The Chicxulub asteroid impact and mass extinction at the Cretaceous–Paleogene boundary. *Science* 327:1214–1218.
- Schuraytz B. C., Sharpton V. L., and Marín L. E. 1994. Petrology of impact-melt rocks at the Chicxulub multiring basin, Yucatán, Mexico. *Geology* 22:868–872.
- Sharpton V. L., Dalrymple G. B., Marín L. E., Ryder G., Schuraytz B. C., and Urrutia-Fucugauchi J. 1992. New links between the Chicxulub impact structure and the Cretaceous/Tertiary boundary. *Nature* 359:819–821.
- Shukolyukov A. and Lugmair G. W. 1998. Isotopic evidence for the Cretaceous–Tertiary impactor and its type. *Science* 282:927–930.
- Simpson S. L., Osinski G. R., Longstaffe F. J., Schmieder M., and Kring D. A. 2020. Hydrothermal alteration associated with the Chicxulub impact crater upper peak-ring breccias. *Earth and Planetary Science Letters* 547:116425.
- Sisson T. W. and Grove T. L. 1993. Temperatures and H₂O contents of low-MgO high-alumina basalts. *Contributions to Mineralogy and Petrology* 113:167–184.
- Smit J. 1999. The global stratigraphy of the Cretaceous–Tertiary boundary impact ejecta. *Annual Review of Earth and Planetary Sciences* 27:75–113.
- Son T. H. and Koeberl C. 2005. Chemical variation within fragments of Australasian tektites. *Meteoritics & Planetary Science* 40:805–815.
- Sprain C. J., Renne P. R., Clemens W. A., and Wilson G. P. 2018. Calibration of chron C29r: New high-precision geochronologic and paleomagnetic constraints from the Hell Creek region, Montana. *Geological Society of America Bulletin* 130:1615–1644.
- Steiner M. B. 2005. Pangean reconstruction of the Yucatan Block: Its Permian, Triassic, and Jurassic geologic and tectonic history. In *The Mojave-Sonora Megashield hypothesis: Development, assessment, and alternatives*, edited by Anderson T. H., Nourse J. A., McKee J. W., and Steiner M. B. Geological Society of America Special Paper 393. Boulder, Colorado: Geological Society of America. pp. 457–480.
- Swisher C. C., Grajales-Nishimura J. M., Montanari A., Margolis S. V., Claeys P., Alvarez W., Renne P., Cedillo-Pardo E., Maurrasse F.-J.-M.-R., Curtis G. H., Smit J., and McWilliams M. O. 1992. Coeval ⁴⁰Ar/³⁹Ar ages of 65.0 million years ago from Chicxulub crater melt rock and Cretaceous–Tertiary boundary tektites. *Science* 257:954–958.
- Timms N. E., Pearce M. A., Erickson T. M., Cavosie A. J., Rae A. S. P., Wheeler J., Wittman A., Ferrière L., Poelchau M. H., Tomioka N., Collins G. S., Gulick S. P. S., Rasmussen C., Morgan J. V., and IODP-ICDP Expedition 364 Scientists. 2019. New shock microstructures in titanite (CaTiSiO₅) from the peak ring of the Chicxulub impact structure, Mexico. *Contributions to Mineralogy and Petrology* 174:38.
- Tuchscherer M. G., Reimold W. U., Koeberl C., and Gibson R. L. 2004a. Major and trace element characteristics of impactites from the Yaxcopoil-1 borehole, Chicxulub structure, Mexico. *Meteoritics & Planetary Science* 39:955–978.
- Tuchscherer M. G., Reimold W. U., Koeberl C., Gibson R. L., and de Bruin D. 2004b. First petrographic results on impactites from the Yaxcopoil-1 borehole, Chicxulub structure, Mexico. *Meteoritics & Planetary Science* 39:899–930.
- Tuchscherer M. G., Reimold W. U., Koeberl C., and Gibson R. L. 2005. Geochemical and petrographic characteristics of impactites and Cretaceous target rocks from the Yaxcopoil-1 borehole, Chicxulub impact structure, Mexico: Implications for target composition. *Meteoritics & Planetary Science* 40:1513–1536.
- Tuchscherer M. G., Reimold W. U., Gibson R. L., de Bruin D., and Späth A. 2006. Major and trace element compositions of melt particles and associated phases from the Yaxcopoil-1 drill core, Chicxulub impact structure, Mexico. *Meteoritics & Planetary Science* 41:1361–1379.
- Urrutia-Fucugauchi J., Marín L., and Trejo-García A. 1996. UNAM scientific drilling program of Chicxulub impact structure—Evidence for a 300 kilometer crater diameter. *Geophysical Research Letters* 23:1565–1568.
- Veizer J. 1989. Strontium isotopes in seawater through time. *Annual Review of Earth and Planetary Sciences* 17:141–167.
- Ward W. C., Keller G., Stinnesbeck W., and Adatte T. 1995. Yucatán subsurface stratigraphy: Implications and constraints for the Chicxulub impact. *Geology* 23:873–876.
- Weber B. and Köhler H. 1999. Sm–Nd, Rb–Sr and U–Pb geochronology of a Grenville Terrane in Southern Mexico: Origin and geologic history of the Guichicovi Complex. *Precambrian Research* 96:145–262.
- Weber B., Valencia V. A., Schaaf P., Pompa-Mera V., and Ruiz J. 2008. Significance of provenance ages from the Chiapas Massif Complex (Southeastern Mexico): Redefining the Paleozoic basement of the Maya Block and its evolution in a Peri-Gondwanan realm. *The Journal of Geology* 116:619–639.
- Weber B., Scherer E. E., Martens U. K., and Mezger K. 2012. Where did the lower Paleozoic rocks of Yucatan come from? A U–Pb, Lu–Hf, and Sm–Nd isotope study. *Chemical Geology* 312–313:1–17.
- Weber B., González-Guzmán R., Manjarrez-Juárez R., de León A. C., Martens U., Solari L., Hecht L., and Valencia

- V. 2018. Late Mesoproterozoic to Early Paleozoic history of metamorphic basement from the southeastern Chiapas Massif Complex, Mexico, and implications for the evolution of NW Gondwana. *Lithos* 300–301:177–199.
- Wittmann A., Kenkmann T., Schmitt R. T., Hecht L., and Stöffler D. 2004. Impact-related dike breccia lithologies in the ICDP drill core Yaxcopoil-1, Chicxulub impact structure, Mexico. *Meteoritics & Planetary Science* 39:931–954.
- Wittmann A., van Soest M., Hodges K. V., Darling J. R., Morgan J. V., Gulick S. P. S., Stockli D., Rasmussen C., Kring D. A., and Schmieder M. 2018. Petrology and radioisotopic ages of allanite in the peak ring of the Chicxulub impact crater (abstract #6286). 81st Annual Meeting of The Meteoritical Society, Moscow, Russia. LPI Contribution 2067.
- Zhao J., Xiao L., Gulick S. P. S., Morgan J. V., Kring D. A., Urrutia-Fucugauchi J., Schmieder M., de Graaff S. J., Wittmann A., Ross C. H., Claeys P., Pickersgill A., Kaskes P., Goderis S., Rasmussen C., Vajda V., Ferrière L., Feignon J.-G., Chenot E., Perez-Cruz L., Sato H., Yamaguchi K., and IODP-ICDP Expedition 364 Scientists. 2020. Geochemistry, geochronology and petrogenesis of Maya Block granitoids and dykes from the Chicxulub impact crater, Gulf of Mexico: Implications for the assembly of Pangea. *Gondwana Research* 82:128–150.

SUPPORTING INFORMATION

Additional supporting information may be found in the online version of this article.

Data S1. Raw geochemical data for major elements, trace elements, and Sr–Nd isotopic analyses.

Fig. S1. Thick sections mosaic scan of selected granite, granite clast granite breccia, and aplite samples

investigated using μ XRF. Three samples were taken from a different interval than the samples used for geochemical investigations; however, they are located very close within few centimeters from each other and thus, the chemical variation should be negligible.

Fig. S2. Bivariate diagrams of V and Zr versus TiO_2 , and La and U versus Zr.
